PLA2G1B is involved in CD4 anergy and CD4 lymphopenia in HIV-infected patients

Julien Pothlichet, Thierry Rose, Florence Bugault, Louise Jeammet, Annalisa Meola, Ahmed Haouz, Frederick Saul, David Geny, José Alcami, Ezequiel Ruiz-Mateos, et al.

TITLE: PLA2G1B IS INVOLVED IN CD4 ANERGY AND CD4 LYMPHOPENIA IN HIV-INFECTED PATIENTS

Authors: Julien Pothlichet[1,10], Thierry Rose[2,10], Florence Bugault[1,3], Louise Jeammet[1], Annalisa Meola[1], Ahmed Haouz[4], Frederick Saul[4], David Geny[5], José Alcami[6], Ezequiel Ruiz-Mateos Carmona[7], Luc Teyton[8], Gérard Lambeau[9], and Jacques Thèze[1,3]

Affiliation : [1]Diaccurate, Institut Pasteur, Paris, France.
[2]Center for Innovation and Technological Research, Institut Pasteur, Paris, France.
[3]Département Santé Globale, Institut Pasteur, Paris, France.
[4]Plate-forme Cristallographie, Institut Pasteur, Paris, France.
[5]NeuraImag Facility, Institute of Psychiatry and Neurosciences of Paris. INSERM U1266, Paris, France.
[6]Unidad de Immunopatología del SIDA, Centro Nacional de Microbiologia, Instituto de Salud Carlos III, ISCIII, Madrid and Hospital Clinic-Institut d'investigations Biomèdiques August i Sunyer (IDIBASPS) Barcelona , Spain.
[7]Laboratorio de Infeccion por VIH y farmacocinetica de antivirales, UGC, Instituto de Biomedicina de Sevilla, Hospitales Universitarios Virgen del Rocio, Sevilla, Spain.
[8]Department of Microbiology and Immunology, Scripps Research Institute, California, USA.
[9]Université Côte d'Azur, CNRS, IPMC, Valbonne Sophia Antipolis, France.
[10]These authors contributed equally: Julien Pothlichet, and Thierry Rose.

Address correspondence to : Jacques Thèze, DIACCURATE, Institut Pasteur, 25 rue du Dr Roux, Bat . ROUX, 2nd Floor, 75015 Paris. Phone : 33.1.45.68.86.00.
Email: Jacques.theze@diaccurate.com

CONFLICT OF INTEREST

J.T. is cofounder and CEO of DIACCURATE, a spin-off of the Institut Pasteur. J.P., L.J. and A.M. are employees of DIACCURATE.

ABSTRACT

The precise mechanism leading to profound immunodeficiency of HIV-infected patients is still only partially understood. Here, we show that more than 80% of CD4 T cells from HIV-infected patients have morphological abnormalities. Their membranes exhibited numerous large abnormal membrane microdomains (aMMDs), which trap and inactivate physiological receptors, such as that for IL-7. In patient plasma, we identified phospholipase A2 group IB (PLA2G1B) as the key molecule responsible for the formation of aMMDs. At physiological concentrations, PLA2G1B synergized with the HIV gp41 envelope protein, which appears to be a driver that targets PLA2G1B to the CD4 T-cell surface. The PLA2G1B/gp41 pair induced CD4 T cell unresponsiveness (anergy). At high concentrations in vitro, PLA2G1B acted alone, independently of gp41, and inhibited the IL-2, IL-4, and IL-7 responses, as well as TCR-mediated activation and proliferation, of CD4 T cells. PLA2G1B also decreased CD4 T-cell survival in vitro, likely playing a role in CD4 lymphopenia in conjunction with its induced IL-7 receptor defects. The effects on CD4 T-cell anergy could be blocked by a PLA2G1B-specific neutralizing mAb in vitro and in vivo. The PLA2G1B/gp41 pair constitutes a new mechanism of immune dysfunction and a compelling target for boosting immune responses in HIV-infected patients.

INTRODUCTION

CD4 lymphocytes play a critical role in the severe immunodeficiency that characterizes HIV-infected patients. Although less than 0.5% of blood CD4 T cells are infected, almost all are dysfunctional. Their progressive decline leads to CD4 lymphopenia. In addition, functional defects of the remaining CD4 T cells lead to their unresponsiveness, or anergy, to certain antigens and cytokines (1). Major progress has been made in treatment of the viral infection. Antiretrovirals (ARVs) prevent acquired immunodeficiency syndrome (AIDS). However, further improvement in HIV therapy will require a better understanding of the mechanisms responsible for CD4 T-cell defects following HIV infection (2, 3).

The mechanism explaining CD4 T-cell loss during HIV infection is still debated (4, 5). Persistent immune activation plays a critical role in the induction of this CD4 T-cell decline (6–8). A major mechanism results from damage of the mucosal barrier and lymphoid tissues of the gastrointestinal (GI) track that follows acute infection. HIV targets subpopulations of CCR5-expressing CD4 T cells, which are dense in the GI. Following this damage, microbial products translocate across the GI barrier and cause general activation of the immune system (9–11). In this context, it is noteworthy that HIV controller patients, who maintain high CD4 counts and good control of viremia, show low inflammation (12).

Numerous investigations have described the impairment of CD4 T-cell function in HIV-infected individuals, in whom CD4 T cells fail to proliferate after stimulation by antigens or mitogens (13, 14). A progressive loss of T helper function has also been reported (15–17). These results may be partially explained by changes in the T-cell receptor repertoire (18), but they may also result from a defect in the intrinsic capacity of the CD4 T cells to respond to physiological signals. For example, a selective defect in IL-2 production, but not IFNγ synthesis, has been reported after anti-CD3 stimulation (19). In this context, we

previously analyzed CD4 T cell responses to IL-2 and IL-7, two cytokines that are crucial for the control of the function, proliferation, and survival of CD4 T cells. We showed that the beta and gamma c (γc) chains of IL-2 receptor (IL-2R) are under-expressed and non-functional, as measured by reduced entry into the S+G2/M phases of the cell cycle (20). Similarly, decreased expression of the IL-7R alpha chain (CD127) on the surface of CD4 T cells from HIV-infected patients has been described and their function was shown to be defective (21). Altered induction of the anti-apoptotic molecule Bcl-2 and decreased expression of CD25 after in vitro exposure to IL-7 were measured (22). We subsequently showed that the Janus kinase (Jak)/Signal Transducer and Activator of Transcription 5 (STAT5) signaling pathway is involved in these defects (23, 24). Similar results involving γc have been published by other investigators (25–30).

Most of the studies performed in lymphocytes from HIV-infected patients have used FACS analysis and in vitro functional immunological assays. Here, we reinvestigated this question by studying purified CD4 T lymphocytes from viremic HIV-infected patients using imaging techniques (31) and molecular approaches rarely used in this field (32–34). We detected large abnormal membrane microdomains (aMMDs) at the surface of CD4 T cells purified from HIV-infected patients in the absence of any stimulation. The aMMD-bearing cells were named "Bumpy T cells", due to their appearance after labeling. Their large aMMDs were shown to trap all IL-7R chains (alpha and γc). IL-7R chains lose their function when embedded in these aMMDs. Consequently, the Jak/STAT pathway was not functional and IL-7-induced phospho-STAT5 nuclear translocation (pSTAT5 NT) was inhibited. Bumpy T cells were recovered after exposure of CD4 T cells from healthy donors (HD) to plasma from HIV-infected patients. After characterization, we found that phospholipase A2 group IB (PLA2G1B) (35) was able to recapitulate the effects of plasma from HIV-infected patients. It induced aMMDs and consequently strongly affected numerous CD4 functions in vitro and in vivo (mouse model).

However, PLA2G1B was found to synergize with HIV gp41 envelope protein in the blood of HIV-infected patients at physiological concentrations. Overall, our results provide new insights into CD4 T-cell dysfunction and a mechanism for the CD4 anergy and lymphopenia observed in chronically HIV-infected patients.

RESULTS

Membrane alterations and signaling defects in CD4 T cells from HIV-infected patients.

Stimulation emission depletion (STED) microscopy revealed numerous large aMMDs (up to 500/cell, with an average size > 200 nm) at the surface of purified CD4 T cells from VP, in the absence of any activation. More than 80% of purified CD4 T cells, also called Bumpy T cells, from all viremic patients (VPs) exhibited aMMDs (Figure 1, A-C). Under the same conditions, resting CD4 T cells from healthy donors (HD) did not spontaneously exhibit any aMMDs, whereas IL-7 stimulation promoted the formation of numerous physiological MMDs (pMMDs) of smaller size (approximately 800/cell, with an average size of 100 nm) (Figure 1, A-C). In contrast, IL-7 stimulation of CD4 T cells from VPs did not induce any observable changes in their membranes (Figure 1, A and B).

We then examined the functional consequences of these morphological changes in the membrane using the IL-7/IL-7R system as a readout. The function of IL-7Rs of VP CD4 T cells was altered, as the IL-7-induced phosphorylation of STAT5 (pSTAT5) differed between CD4 T cells of HDs and VPs (Figure 1D); pSTAT5 nuclear translocation (pSTAT5 NT) was almost completely abolished in the CD4 T cells from VPs after IL-7 stimulation. This resulted from the difference in the kinetics of cytoplasmic phosphorylation of STAT5 and pSTAT5 NT between CD4 T cells of VPs and HDs (Figure 1E).

We previously showed that IL-7-induced cytoskeletal organization is required for efficient pSTAT5 NT in CD4 T cells of HDs and that colchicine and cytochalasin D treatment abolishes

pSTAT5 NT (34). These results are comparable to those obtained for non-treated VP CD4 T cells (Supplemental Figure 1, A and B). Microfilaments and microtubules can be observed after IL-7 stimulation. Due to the very small size of the cytoplasm of lymphocytes, these structures were observed by pulsed STED microscopy. After staining by anti-tubulin antibodies, microtubules could be observed in HD CD4 T cells but not VP CD4 T cells (Supplemental Figure 1C). Similarly, microfilaments were visible in HD CD4 T cells after staining by anti-actin antibodies but not in VP CD4 T cells (Supplemental Figure 1D). This further supports that the IL-7/IL-7R system is nonfunctional in VP CD4 T cells.

Overall, these results confirm and structurally characterize the activation status of CD4 T lymphocytes from VPs and provide a new insight into the mechanism of unresponsiveness of these CD4 T cells.

Biochemical analysis of aMMDs from the CD4 T lymphocytes of VPs.

We further examined the mechanism linking the presence of aMMDs at the surface of the CD4 T lymphocytes from VPs and the loss of function of the IL-7/IL-7R system by performing a biochemical analysis of their membranes. Cell lysates obtained after moderate detergent treatment were examined on sucrose gradients. This technique allowed us to separate free molecules which migrate in high-density fractions and the detergent-resistant membranes (DRMs), structurally related to MMDs, which are recovered in the low-density fractions. Flotillin-1 was found in both fractions and was used as a marker in these experiments (Figure 2A and Supplemental Material). IL-7Rα chains and γc chains were found as free molecules in the high-density fractions of HD CD4 T-cell lysates. They were found in low-density DRMs only after IL-7 stimulation (Figure 2A). In contrast, IL-7Rα chains and γc chains were spontaneously found associated with the low-density DRMs in lysates prepared from the Bumpy T cells of VPs, in the absence of any stimulation (Figure 2A). IL-7Rα appeared as

clusters in STED images of the CD4 T-cell membranes from VPs (Figure 2B), further supporting the presence of low-density DRMs containing IL-7R chains. We further verified that IL-7Rα is included in aMMDs by studying its diffusion rate at the membrane surface. IL-7Rα was included in the aMMDs of VP CD4 T cells, as their diffusion was limited and could be restored after disruption of the aMMDs by cholesterol oxidase and sphingomyelinase treatment (Figure 2, C and D).

Overall these results demonstrate that IL-7Rα and γc are spontaneously embedded in specific macrostructures of the membranes of CD4 T cells from VPs, measured as aMMDs or DRMs. These data also show that the receptors lose their function when trapped in this abnormal structure of Bumpy CD4 T cells.

Plasma from VPs induces the Bumpy T-cell phenotype in HD CD4 T cells.

We investigated the molecular mechanism leading to the Bumpy T-cell phenotype. The addition of plasma from VPs (Figure 3A) to HD CD4 T cells was sufficient to induce the Bumpy T-cell phenotype. Titration showed the phenotype to be induced in 50% of the cells at approximately 1% VP plasma (Figure 3B). HD CD4 lymphocytes treated with VP plasma and Bumpy T cells were microscopically undistinguishable, and the number and size of aMMDs at their surface were not influenced by IL-7. In addition, plasma from elite controllers (HICp) (36, 37) and patients with suppressed viremia after 10 years of ARV (ARTp) could not induce this phenotype (Figure 3B).

We then studied the responsiveness of VP plasma-induced Bumpy T cells. IL-7-induced pSTAT5 NT was inhibited by VP plasma, with a half maximum dose of 1% (Figure 3, C and D). These results suggest a direct link between the induction of aMMDs and the mechanism leading to the inhibition of pSTAT5 NT. We found a positive correlation between the number

of pMMDs and the frequency of cells with translocated pSTAT5 during IL-7 responses in HD CD4 T cells (Figure 3E). Conversely, we found a negative correlation between the number of aMMDs per CD4 T cell and the percent of cells with nuclear pSTAT5 in IL-7-stimulated plasma-induced Bumpy T cells (Figure 3F). These correlations further support that plasma-induced aMMDs are responsible for the loss of IL-7 response.

Phospholipase A2 group IB (PLA2G1B) is a unique inducer of Bumpy T cells.

We biochemically characterized the plasma molecule involved in these morphological and functional changes. Size-exclusion and ion exchange chromatography were used to determine the apparent MW and pI of the bioactive molecule(s) from the plasma of three VPs, using microscopy as a read-out (Supplemental Figure 2, A-C). A list of 103 10-15 kDa proteins with a pI between 6.5 and 7.5 and a secretory signal peptide was determined. Differential mass spectrometry analysis identified PLA2G1B, also known as pancreatic phospholipase (35), as the top candidate (PA21B in Supplemental Figure 2D). Active PLA2G1B is produced after the cleavage of seven N-terminal residues from non-active proPLA2G1B (38). Recombinant PLA2G1B was produced, purified, crystallized and structurally characterized. The position of residues H48 and D99 and the Ca^{2+}-binding loop, critical for the activity of the enzyme, are shown in Figure 4A.

Recombinant PLA2G1B alone was able to induce aMMDs (Figure 4B) and inhibit pSTAT5 NT in HD CD4 T cells (Figure 4C). This property was catalytic site-dependent, as the non-active H48Q mutant (39) was unable to induce aMMDs or inhibit pSTAT5 NT on human CD4 T cells (Figure 4, D and F). These effects were specific to PLA2G1B; indeed, other members of the PLA2 family such as PLA2GIIA, PLA2GIID or PLA2GX showed no significant effect on either aMMDs formation or pSTAT5 NT inhibition (Figure 4, E and G). Similarly, only polyclonal antibodies specific for PLA2G1B decreased plasma-induced pSTAT5 NT

194 inhibition, whereas polyclonal antibodies specific for PLA2GIIA or PLA2GIID had no effect
195 (Figure 4H).

196 We developed mouse monoclonal antibodies (mAb) specific for PLA2G1B. Among them, mAb
197 14G9 efficiently inhibited the enzymatic activity of PLA2G1B and abrogated VP plasma-
198 inhibition of pSTAT5 NT in a dose-dependent manner (Figure 4I). These experiments show
199 that, at physiological concentrations, PLA2G1B is involved in the phenotypic and functional
200 changes induced by VP plasma in HD CD4 T cells and the Bumpy T-cell phenotype observed
201 in VP.
202
203 *PLA2G1B induces anergy of CD4 T cells: specificity and reversal of the effects.*
204 The unresponsiveness of CD4 T cells to IL-7 induced by PLA2G1B was also observed for IL-
205 2 and IL-4, two other γc cytokines. Similar to IL-7, pSTAT NT-induced by these two cytokines
206 was inhibited by PLA2G1B in a dose-dependent manner and with a comparable IC50 (Figure
207 5A). These observations were verified using VP plasma-induced Bumpy T cells (Figure 5B).
208 Unlike IL-2, IL-4, and IL-7, IFNα-induced pSTAT1 NT was not inhibited by PLA2G1B or the
209 plasma of VPs (Figure 5, C and D). IFN-α is known to signal by a mechanism independent of
210 MMDs (40, 41). Thus, these results suggest that PLA2G1B only affects signaling pathways that
211 involve compartmentalization into pMMDs. We then studied the effects of PLA2G1B first
212 observed on total unseparated CD4 T cells, on naïve ($CD45RA^+$) and memory ($CD45RA^-$) CD4
213 T cells. PLA2G1B was slightly more active on $CD45RA^+$ CD4 T cells than $CD45RA^-$ CD4 T
214 cells (Figure 5E). Such differential sensitivity is not the consequence of selective modulation
215 of IL-7R (CD127) expression at the cell surface by PLA2G1B (Figure 5, F and G and
216 Supplemental Figure 3). As previously described, the percentage of CD127-positive cells was
217 slightly higher in $CD45RA^+$ than $CD45RA^-$ CD4 T cells (Figure 5F) (42, 43). In addition MFI
218 analysis of CD127 expression (Figure 5G and Supplemental Figure 3) showed a slight reduction

in CD45RA- cells as previously reported (44). Overall, these analyses establish that PLA2G1B does not influence CD127 expression and support our hypothesis that PLA2G1B acts on signal transduction (as described above) and not by decreasing receptor expression.

The action of PLA2G1B appears to be specific to CD4 T cells. Indeed, PLA2G1B did not induce aMMD formation in purified CD8 T cells from HDs (Figure 5H). Similarly, pSTAT5 NT was not affected in CD8 T cells by PLA2G1B, even at high concentrations (Figure 5I). These results are consistent with ex vivo observations of VP CD8 T cells in which aMMDs were not detectable and pSTAT5 NT continued to occur (Supplemental Figure 4, A-C). In addition, physiological concentrations of PLA2G1B present in VP plasma inhibited pSTAT5 NT on CD4 T cells but had no functional effects in CD8 lymphocytes purified from HDs (Supplemental Figure 4D).

PLA2G1B is known to digest lipids, we thus further explored the difference between the response of CD4 and CD8 T cells to PLA2G1B by lipidomic analysis. There were significant differences in the proportions of the ganglioside GM3, PC, PE, PI, PS, SM and TG between HD CD4 and CD8 T cells (Supplemental Figure 4E). Similarly, differences in the lipid proportions have been reported between murine CD4 and CD8 T cells (45). It is possible that the differential effects of PLA2G1B on CD4 and CD8 T cells are associated with differences in lipid composition, but direct evidence will require extensive studies.

We next investigated the reversal of the induced Bumpy T-cell phenotype in vitro and show the results of one of three representative experiments (Figure 5J). Purified CD4 T cells were first treated in vitro with PLA2G1B and then cultured for various periods of time up to 3 days. Inhibition of pSTAT5 NT was examined every day. Under our experimental conditions, 30% of the cells were anergized and did not respond to IL-7. After three days in culture, pSTAT5

NT returned to normal, clearly showing that the Bumpy T-cell phenotype is reversible. Furthermore, neutralizing mAb 14G9 accelerated the reversion (Figure 5J).

PLA2G1B affects CD4 T-cell survival in vitro: inhibition by neutralizing mAb 14G9.

Aside from the unresponsiveness of CD4 T cells to physiological signals (anergy), HIV-infected patients suffer from CD4 lymphopenia. We thus tested the effects of PLA2G1B on the half-life of CD4 T cells in vitro. Purified CD4 lymphocytes were cultured and the number of live cells counted over time as described in Methods. The number of surviving CD4 T cells varied between donors in control cultures. The effects of PLA2G1B on the CD4 lymphocytes are thus expressed as the percentage of the surviving cells relative to that in control cultures in the absence of PLA2G1B at each time point. The effect of PLA2G1B on CD4 T-cell survival was first tested at various concentrations up to 100 μM (Figure 6A). We then verified that 50% cells died after 18 days of culture in the presence of 1 μM PLA2G1B (Supplemental Figure 5A) and 40% of the cells died after 24 days of culture in the presence of 250 nM PLA2G1B (Figure 6B).

During these experiments, we further analyzed the CD4 T cells. As expected, numerous dying cells become Annexin V-positive Zombie-positive. However, we also detected Annexin V-negative Zombie-positive cells (Figure 6, C and D). Their percentage increased during culture, reaching more than 70% of the recovered lymphocytes (Figure 6E). This was a specific consequence of PLA2G1B treatment, as such cells were not detected when CD4 T cells were cultured in the presence of the inactive PLA2G1B mutant H48Q (Figure 6C and Supplemental Figure 5B). Similarly, their percentage was lower when cultures were performed in the presence of mAb 14G9, which neutralizes the enzymatic activity of PLA2G1B (Figure 6, D and E). This can be explained by the fact that PLA2G1B digested one of its substrates during culture,

phosphatidylserine, which is also the binding site of Annexin V. This confirms that the action of PLA2G1B on CD4 T cells is mediated by its enzymatic activity.

We then tested the effect of mAb 14G9 on CD4 T-cell survival. The mAb significantly increased the survival of CD4 T cells exposed to PLA2G1B (up to > 50%) relative to cultures in the presence of the control isotype (Figure 6F and Supplemental Figure 5C).

In vitro and in vivo effects of human PLA2G1B in a mouse model.

We studied the effects of human PLA2G1B in mice after verifying its activity in vitro on mouse CD4 T cells to extend our data in vivo. Upon exposure to PLA2G1B we also observed Annexin V-negative Zombie-positive mouse CD4 T cells (Supplemental Figure 6). CD4 T cells from C57BL/6 mice were purified from the spleen and stimulated by anti-CD3 plus anti-CD28 beads, in the presence of IL-2. Human PLA2G1B was active on mouse CD4 T cells and induction of CD25 (IL-2Rα) was inhibited by PLA2G1B by day 5 in a dose-dependent manner (Figure 7, A and B). Similarly, survival and proliferation were profoundly altered (Figure 7, C-E). These effects depended on the catalytic activity of PLA2G1B, as the H48Q mutant was ineffective (Figure 7, A-E). Furthermore, neutralizing mAb 14G9 blocked CD25 induction and decreased survival of the CD4 cells (Figure 7, F and G). These data demonstrate that PLA2G1B can also inhibit TCR responses. In addition to the human experiments, these data establish that the effects of PLA2G1B can be measured after several days in culture.

In vivo, PLA2G1B showed activity on mouse CD4 lymphocytes in a dose-dependent manner (Figure 7H). Injection of 100 μg of PLA2G1B induced a long-lasting effect, which persisted for up to 72 hours and began to diminish after 168 hours (Figure 7I). The effect of PLA2G1B was maximal three hours after injection (Figure 7J). We tested the effects of pre-treatment with the anti-PLA2G1B neutralizing mAb 14G9 under the same experimental conditions (Figure

7K). The blockade was close to 100%. We obtained a comparable result in a group of mice that was pre-immunized against human PLA2G1B (Figure 7L).

The cell specificity of the effects of PLA2G1B was further verified in this experimental model. Injection of PLA2G1B did not result in any loss of IL-7-induced pSTAT5 NT in mouse CD8 lymphocytes, as measured ex vivo three hours post-injection (Supplemental Figure 4F). Overall, these results open the possibility of using mouse models to evaluate anti-PLA2G1B neutralizing mAbs as an immunotherapeutic strategy.

Synergy between PLA2G1B and plasma HIV gp41 protein.

We then measured active and proPLA2G1B in the plasma of HD, HIC, ARV, and VP patients using PLA2G1B ELISAs (Figure 8, A and B). VPs had similar levels of active PLA2G1B as HIC and ART patients but slightly more active PLA2G1B than HDs (median increase of 1.4). In addition, comparable copy numbers of *pla2g1b* RNA were found in the PBMCs of HDs and VPs by qPCR (Figure 8C). We thought that these results cannot explain the difference in PLA2G1B activity observed with the functional assays (Figure 3, B and D). This observation led us to consider that one or more cofactors are present in the plasma of VPs and are required for the induction of aMMDs and blockade of pSTAT5 NT. Indeed, the dose-response curve (from 0.001 to 1,000 nM) of PLA2G1B diluted in HD or VP plasma previously depleted of endogenous PLA2G1B showed striking differences in the IC50 values (Figure 8D), supporting the presence of a cofactor. The IC50 of PLA2G1B was 75 nM when diluted in PBS buffer or HD plasma, but decreased to 5 nM when diluted in PLA2G1B-depleted VP plasma. We concluded that PLA2G1B was not acting alone but in synergy with another factor present in VP plasma. A bioassay was developed, using a limiting amount of PLA2G1B inactive by itself (5 nM, Figure 8D) and PLA2G1B-depleted VP plasma to detect the potential cofactor (Figure 8E), and used to show that the enhancement was lost after plasma was incubated with purified

CD4 T cells (Figure 8F), suggesting that the cofactor was adsorbed on CD4 T cells. After such pretreatment, the addition of 5 nM PLA2G1B to the CD4 T cells, without further addition of VP plasma, resulted in the inhibition of IL-7 driven pSTAT5 NT (Figure 8G). This cofactor activity was sensitive to trypsin treatment and could be fractionated with an apparent MW between 10 and 30 kDa. The search then focused on HIV peptides possibly released into the plasma of infected patients. A gp41 fragment (MN 565-771 delta 642-725), and its corresponding 3S peptide (46), of which the sequence is highly conserved among various HIV isolates, exerted strong cofactor activity (Figure 8, H-K). In addition, the depletion of VP plasma with anti-gp41-specific antibodies that do not bind to gp120 (Supplemental Figure 7) resulted in the loss of cofactor activity (Figure 8L). This critical point was definitively established after depletion by a mAb characterized in the laboratory. This mAb, 1C5, was raised against the 3S peptide and shown to also recognize gp41 protein but not gp120 (Supplemental Figure 7). It was also able to completely deplete various VP plasma samples of cofactor activity (Figure 8M). These results support the hypothesis that fragments of gp41 containing the 3S sequence may act as cofactors that target PLA2G1B to the surface of CD4 lymphocytes to exert its enzymatic activity.

DISCUSSION

Here, we further characterize the activation status of the CD4 T-cell compartment in HIV-infected patients. Aside from currently used cell-surface activation markers, such as CD38 and HLA-DR, we show structural alterations of CD4 T-cell membranes, consisting of large aMMDs observed at the cell surface. They arise due to the activity of the PLA2G1B enzyme, acting in synergy with gp41. These findings support a new mechanism of immunosuppression in HIV-infected patients. Here, we show that this mechanism is involved in CD4 anergy to γc cytokine

and TCR responses. Furthermore, its action on the decreased survival of CD4 T cells suggests a role in CD4 lymphopenia.

Bumpy T cells represent a new phenotype characterizing activated CD4 T cells found in HIV-infected patients. It results from remodeling of the CD4 T-cell membrane under the influence of the enzymatic activity of PLA2G1B. This exposes GM1 gangliosides, which are enriched in aMMDs and recognized by labeled cholera toxin B using the STED imaging technique. Bumpy T cells expressing numerous aMMDs up to 500/cell can be recovered from patient blood and easily identified. In the blood of these individuals, aMMDs are spontaneously expressed by CD4 T cells and their characteristic pattern is not modified by a strong stimulus, such as IL-7. Given that this phenotype is observed in more than 80% of the CD4 T cells of HIV-infected patients, a correlation with CD38 and HLA-DR activation markers should be investigated. In any case, this observation offers new insights into our understanding of the dysfunction of the CD4 compartment of HIV-infected patients.

At low concentrations, such as those found in the blood, PLA2G1B cannot act by itself. In HIV-infected patients, it requires a cofactor, which we identified as a soluble fragment of gp41. Gp41 appears to be a driver that targets PLA2G1B to the CD4 T-cell surface. Molecular dissection of gp41 demonstrated that the 3S peptide of gp41 is the active moiety. Plasma gp41 is most likely a degradation product of circulating HIV or HIV-infected dead cells. We analyzed the spatiotemporal mode of action of these two molecules when in the plasma. Our results suggest that they act in two separate steps. Gp41 acts first and possibly modifies the CD4 membrane. Gp41 may bind to CD4 T-cell membranes by binding to the gC1qR through its 3S sequence (47, 48). This may change the membrane composition, possibly through induction of the fusion of exocytic vesicles with the plasma membrane, as previously shown for NKp44L induction (47). In the second step, these changes in lipid composition of the outer leaflet of the CD4 T-

363 cell may increase the binding and activity of PLA2G1B (49), making the modified membrane
364 a target of PLA2G1B.

365 PLA2G1B is the active moiety of the PLA2G1B/gp41 pair. At high concentrations, it appears
366 to act, in the absence of gp41, as a newly discovered immune modulator that acts on CD4 T
367 cells. Its unique properties, under these conditions, were defined in vitro or in vivo in mouse
368 experiments. PLA2G1B induces numerous aMMDs, trapping and inactivating the function of
369 receptors (γc family, TCR,…), thus decreasing physiological activation, proliferation, and
370 survival. The results obtained with IFNα show that PLA2G1B works selectively on systems
371 that use pMMDs for physiological signaling. It is possible that, by digesting phospholipids,
372 PLA2G1B modifies membrane composition and changes its fluidity, allowing pMMDs to fuse
373 and form receptor-inactivating aMMDs.

374 Despite this broad activity, the action of PLA2G1B remains specific and does not act directly
375 on CD8 T cells. However, this mechanism may indirectly affect CD8 responses in HIV-infected
376 patients, which are mostly highly CD4 T cell-dependent (50). It will be of interest to extend our
377 studies to other immune cells, such as NK cells, which are highly dependent on the γc cytokine
378 IL-15 for their activity (51).

379 In this context, we sought the origins of active PLA2G1B in the blood. We found the pancreas
380 to be a major source of PLA2G1B, followed by the duodenum, jejunum, and ileum
381 (Supplemental Figure 8, A-C). We used two different mAbs, 1C11 recognizing both
382 proPLA2G1B and active PLA2G1B and 14G9 specific for the active form, and observed that
383 proPLA2G1B is expressed in the endocrine pancreas while active PLA2G1B is mainly
384 expressed in the exocrine pancreas and intestinal tissues. We also observed low amounts of
385 *pla2g1b* transcripts in lymphoid cells (CD4 or CD8 T cells and Natural Killer cells) by qPCR,
386 whereas they were almost undetectable in myeloid cells (lung macrophages, mDC and pDC

dendritic cells) (Supplemental Figure 8D). The mechanism leading to the presence of active and proPLA2G1B in the blood is still unknown. They may leak from the intestinal tract, where proPLA2G1B is probably cleaved to form active PLA2G1B by proteolytic enzymes. Conversion of proPLA2G1B into the active molecule may also take place at immune sites where inflammatory cells produce proteolytic enzymes. Initially PLA2G1B was thought to play solely a digestive role (35). Because of its function as an immunomodulator, demonstrated here, it may also play a crucial role in the regulation of the lymphoid compartment of the gut immune system. It may be involved in tolerance towards food and microbiota-derived components (52). There is a high level of *pla2g1b* RNA in duodenum (Supplemental Figure 8A) and a high concentration of active PLA2G1B protein in the intestinal lumen (Supplemental Figure 8B). Thus, it may act directly on CD4 T cells or, alternatively, cofactors derived from bacteria or viruses of the microbiota may be involved. These hypotheses may open new challenging areas of investigation.

Our results also have other consequences for our understanding of the immunodeficiency of HIV-infected patients. They show PLA2G1B to be the active component of the PLA2G1B/gp41 pair and to contribute to the processes that renders most of the major conventional CD4 T-cell subpopulations anergic. First, we have clearly demonstrated dysfunction of the IL-7R/IL-7 induced microtubule and microfilament reorganization, therefore blocking pSTAT5 NT. Furthermore, all γc cytokines lost their function because of sequestering of the γc chains in macro-MMDs (aMMDs). This was verified by studying the blockade of IL-2- and IL-4-induced pSTAT NT after PLA2G1B treatment. Furthermore, the TCR responses induced by anti-CD3/anti-CD28 were also inhibited after PLA2G1B treatment. Inhibition of the function of γc cytokines and TCR responses leads to the blockade of antigen-specific responses. Overall, our results show that Bumpy T cells obtained in vitro are anergic and strongly suggest that the same is true for Bumpy T cells recovered from HIV-infected patients.

412 Furthermore, our data suggest that PLA2G1B is also involved in the CD4 lymphopenia
413 observed in HIV-infected patients. IL-7 is the main cytokine that controls homeostasis of the
414 CD4 compartment (53, 54). Thus, the PLA2G1B-induced defect of the IL-7R signaling
415 mechanism described here should significantly contribute to CD4 lymphopenia. Furthermore,
416 the number of surviving CD4 lymphocytes decreased after exposure to PLA2G1B in culture
417 (Figure 6, A and B). During these in vitro studies, we found numerous Annexin V-negative
418 Zombie-positive CD4 T-cells, which can be considered to be the direct consequence of
419 PLA2G1B activity, as they indicate the degradation of phosphatidylserine at the surface of the
420 dying cells (Figure 6, C-E). The activity of PLA2G1B on the membrane of dying cells led to
421 hypothesize an additional role of PLA2G1B in the removal of damaged cells, as previously
422 described for sPLA2 (35, 49). This may also contribute to the decreased in CD4 T-cell number.
423 In the future, Annexin V-negative dying cells could be used as a signature to study the effects
424 of PLA2G1B on the CD4 T cells of HIV-infected patients. This could be used to verify the
425 activity of PLA2G1B in vivo and to follow its neutralization after anti-PLA2G1B
426 immunotherapy.

427 PLA2G1B may represent a compelling therapeutic target for boosting immune responses in
428 people contaminated by HIV. In this context, the potential of the specific mAb 14G9 has to be
429 considered. It completely neutralized the effects of PLA2G1B in vitro, as measured by the
430 inhibition of pSTAT5 NT. This property was also verified in vivo, using a mouse model.
431 Furthermore, 14G9 accelerated the reversion of Bumpy cells in vitro, as measured by their
432 capacity to recover an IL-7 response. It also significantly reduced (up to >50%) the capacity of
433 PLA2G1B to decrease cell survival in vitro. Thus, neutralization of the deleterious effects of
434 the PLA2G1B/gp41 pair may be considered as a new therapeutic tool. It should be able to boost
435 the immune system early in infection, at a time when PLA2G1B is pathogenic as a consequence
436 of its synergy with gp41. Treatment during the beginning of ARV therapy, at a stage when the

viral load remains detectable, may increase the CD4 T cell-dependent immune defense and improve the control of HIV infection. In addition, anti-PLA2G1B therapy could have positive effects in patients infected by ARV-resistant HIV strains. After humanization, 14G9 could be a drug candidate that could be used to boost the functions of the CD4 compartment and the CD4-dependent immune responses of HIV-infected patients. By restoring IL-7 responses, decreasing anergy, and contributing to an increase in CD4 counts, neutralization of PLA2G1B may be one of the critical parameters towards remission of HIV infection (55–57).

The in vivo relevance of our data needs to be further underscored. The most significant data comes from the analysis of the role of plasma from VPs. PLA2G1B in VP plasma is at physiological concentrations and, in the presence of gp41, induces unresponsiveness of CD4 lymphocytes. The activity of plasma from VPs is well established. At the morphological level, Bumpy T cells directly purified from the blood of VPs are indistinguishable from in vitro VP plasma-induced Bumpy T cells. At the functional level, we found that aMMDs characterized from purified CD4 T cells trap all γc chains and subsequently showed that HD CD4 T cells treated with VP plasma become unresponsiveness to γc cytokines, such as IL-2, IL-4, and IL-7 (Figure 5, A and B). Inhibition or depletion of either PLA2G1B or gp41 abolishes the activity of VP plasma (Figure 4, H and I and Figure 8, L and M). We thus propose a mechanism whereby PLA2G1B is the active moiety and gp41 a cofactor or driver that targets PLA2G1B to the surface of CD4 T cells. The activity of the VP plasma results from synergy between the two molecules.

We then analyzed PLA2G1B and gp41 separately in vitro to understand the respective roles of the two molecules. At high concentrations, PLA2G1B is active alone. High concentrations appear to compensate for the absence of gp41. This allows characterization of the biochemical and immunological properties of the active molecule. More significantly, at low concentrations,

cloned PLA2G1B was not active and did not induce unresponsiveness of the CD4 lymphocytes in the absence of gp41. Under these experimental conditions, we clearly show that gp41 boosts PLA2G1B activity (Figure 8, H-K). PLA2G1B becomes pathogenic only after CD4 lymphocytes have interacted with the gp41/3S peptide (Figure 8). Therefore, this in vitro analysis further supports the model that synergy with viral gp41 is required to observe the effects of low concentrations of PLA2G1B.

In addition, studies of three clinical settings confirm the relevance of our observations. PLA2G1B activity strictly correlated with the presence of HIV particles. We only found PLA2G1B activity in VPs who had HIV particles in the circulating blood and therefore gp41 in the plasma. In contrast, HIV controllers and patients treated for more than 10 years with ARV, with an undetectable viral load in their plasma, had no detectable PLA2G1B activity. Furthermore, we observed a negative correlation between the ability of plasma to induce aMMDs in vitro and the CD4 counts of the patient source of plasma in a preliminary analysis (Supplemental Figure 9A). Similarly, plasma from patients with CD4 counts below 300/mm^3 more strongly inhibited pSTAT5 NT than plasma from patients with CD4 counts above 300/mm^3 (Supplemental Figure 9B). Overall, these results corroborate the notion of a viral cofactor/driver that synergizes with PLA2G1B to induce CD4 T lymphocyte unresponsiveness in vivo.

It is noteworthy that the PLA2G1B/gp41 pair appears to be a new mechanism of immunopathology, in which a physiological enzyme becomes pathogenic in the presence of molecules derived from the pathogen. This system may play a role in diseases in which immunodeficiency contributes to the emergence or progression of the disease. Preliminary data obtained with hepatitis C, *Staphylococcus aureus*, and *Porphyromonas gingivalis* support this concept.

METHODS

Characterization of membrane microdomains (MMDs) in primary human CD4 and CD8 T cells.

Cell preparation and labelling of specific proteins were performed as previously described (34). Briefly, purified cells were equilibrated in RPMI with 5% FBS for 2 h at 37°C and 5% CO_2 before plating them onto poly-L-lysine-coated coverslips for 20 min at 37°C. Cells were treated with IL-7 (2 nM, 15 min, 37°C) then fixed with 1.5% paraformaldehyde (PFA, Electron Microscopy Sciences) and rehydrated for 15 min in PBS/5% FBS. GM1 gangliosides were labelled with AlexaFluor-coupled cholera toxin subunit B (CtxB-AlexaFluor488, C22841; CtxB-AlexaFluor633, C34778; or CTxB-Biotin, C34779 and Streptavidin-AlexaFluor647, S32357, Life Technologies).

MMDs were analyzed at the surface of fixed CD4 T cells and CD8 T cells from viremic patients (VPc) and healthy donors (HDc) in response to IL-7 stimulation or not (Figure 1, A-C and Supplemental Figure 4) or purified HD CD4 or CD8 T cells upon treatment with plasma samples (from HD, VP, ART, or HIC), WT or H48Q PLA2G1B, PLA2GIIA, PLA2GIID, or PLA2GX recombinant proteins for 30 min and stimulation with the cytokine for 15 min (Figures 3 to 5).

Images were acquired below the diffraction limit using a Leica TCS STED-CW (31) (Figures 1 and 3 and Supplemental Figure 1) or Leica TCS SP8 STED 3X (Figure 4B) or above the diffraction limit using an inverted laser scanning confocal microscope (LSM700, Zeiss or LSM780 ELYRA PS.1, Zeiss) as previously described (34). Deconvolution was performed using Huygens Pro software (Scientific Volume Imaging, Hilversum, The Netherlands). For each condition, the top half of a representative CD4 T cell is shown from Z-stack images. MMDs were counted on the entire surface of the purified CD4 T cells; an average of 50 cells

were examined for HD and between 15 to 50 for VP. We determined the number of MMDs in Figures 1 and 3 or the percentage of cells with aMMDs on their surface in Figures 4 and 5.

Phosphorylation and nuclear translocation of STAT (pSTAT NT).

STAT phosphorylation and nuclear translocation in VP and HD CD4 T cells were analyzed by microscopy after IL-7 stimulation (2 nM), or in HD CD4 and CD8 T cells incubated with plasma samples from HD, VP, ART, or HIC (30 min), WT or H48Q PLA2G1B, PLA2GIIA, PLA2GIID, or PLA2GX recombinant proteins, with or without neutralizing antibodies (30 min) before a 15 min stimulation with 2 nM IL-7, IL-2, or IL-4 or 1 nM IFN-α2. WT and H48Q porcine PLA2G1B were used for the experiments shown in Figure 4D and F. The effect of the anti-PLA2G1B 14G9 mAb on the recovery of a functional pSTAT5 NT response was studied by pretreating CD4 T cells for 1 h with 250 nM PLA2G1B before the addition of 667 nM anti-PLA2G1B mAb (14G9). All pre-treatments and stimulations were performed at 37°C. Stimulation was stopped by addition of 4% PFA and incubation for 15 min at 37°C. Cells were then permeabilized overnight at -20°C in a 90% methanol/water solution.

CD4 and CD8 T cells were stained using respectively anti-human CD4 (mouse anti- CD4 clone RPA-T4, 555344, BD Biosciences; or goat anti-CD4, AF-379-NA, R&D/Novus) and anti-human CD8 (mouse anti-CD8 clone RPA-T8, 555364, BD Biosciences), labelled with donkey anti-mouse-AlexaFluor488 (A21202, Thermofisher) or donkey anti-goat-AlexaFluor488 (A11055, Thermofisher). Phosphorylation of STAT5 in response to IL-2 or IL-7 stimulation was then revealed by staining with rabbit anti-pSTAT5 (9356, Cell Signaling Technology) labelled with goat anti-rabbit-Atto 647N (15068; Active Motif) or donkey anti-rabbit AlexaFluor555 (A31572, Life Technologies), that of STAT6 in response to IL-4 stimulation by rabbit anti-pSTAT6 (9361, Cell Signaling Technology) labelled with anti-rabbit-AlexaFluor488 (A11034 or A21206, Life Technologies), and that of STAT1 in response to

IFN-α2 stimulation by rabbit anti-pSTAT1 (9167, Cell Signaling Technology) labelled with anti-rabbit-AlexaFluor 488 (A11034 or A21206, Life Technologies).

Images were acquired below the diffraction limit with a DM16000CS/SP5 inverted laser scanning confocal microscope using pulsed excitation STED (TCS STED, Leica) (58) or above the diffraction limit using an inverted laser scanning confocal microscope (LSM700 or LSM780 ELYRA PS.1, Zeiss) as previously described (34). Deconvolution was performed using Huygens Pro software (Scientific Volume Imaging, Hilversum, The Netherlands). The appearance of pSTAT was measured using ImageJ software. pSTAT5 was quantified in the cytoplasm and nucleus of the cells (Figures 1 and 3 and Supplemental Figure 1) where indicated. The number of cells positive for nuclear pSTAT among > 200 in response to cytokines was analyzed by confocal microscopy in Figures 4, 5, 7, and 8 and Supplemental Figure 4.

Study of the effect of PLA2G1B on human CD4 T-cell survival

Purified CD4 T cells were cultured ($7x10^6$ cells/mL) in RPMI 1640 medium supplemented with 5% FBS (Life Sciences – Gibco). FBS was initially selected for its capacity to support efficient CD4 T-cell activation in response to anti-CD3/CD28 stimulation, as measured by CD69 cell-surface expression. The same FBS was also later found to support long-term survival of these lymphocytes. CD4 T cells were treated with PBS, PLA2G1B, or the inactive mutant H48Q PLA2G1B alone or with the anti-PLA2G1B mAb 14G9 (Figure 6 and Supplemental Figure 5) or control isotype (Mouse IgG1, 16-4714-85, Thermofisher, Figure 6 and Supplemental Figure 5). The effect of PLA2G1B on CD4 T-cell survival was evaluated by a Moxy Z Mini Automated Cell Counter (Moxy Z, Orflo technologies). Moxy Z measures cell counts, cell size, and cell health. Cell heath is evaluated via the Moxy Viability Index (MVI) value (59). The results based on the MVI were analogous to those obtained by hemocytometer count of cells stained with

Trypan blue (0.1%).

For the Annexin V experiments, CD4 T cells were stained with AlexaFluor488-labelled antibodies against CD4 (300519, Biolegend) for 30 min at 4°C, the Zombie Violet Fixable Viability Kit (0.5 µL/test) (423114, Biolegend) and Annexin V-APC (5µL/test) (640941, Biolegend) for 15 min at RT. Cells were analyzed with a cytoflex cytometer (Beckman Coulter) and FlowJo software, version 10 (Tree Star).

Determination of gp41 and 3S plasma cofactor peptide activity on healthy donor CD4 T cells. The effect of gp41 on PLA2G1B activity on CD4 T cells was assessed by incubating purified CD4 T cells in PBS/1% BSA containing peptides, recombinant proteins, VP or HD plasma, or the 10-30 kDa fraction previously depleted, or not, of PLA2G1B or gp41 (Supplemental Material), together with recombinant PLA2G1B.

The binding of the viremic plasma cofactor to CD4 T cells was tested by first incubating the PLA2G1B-depleted plasma with CD4 T cells for 15 min. Then, the adsorbed plasma was collected and incubated with other CD4 T cells from the same donor for 30 min, alone or together with PLA2G1B (Figure 8F).

The pretreatment effect of viremic plasma cofactor on CD4 T cells was tested by first incubating the PLA2G1B-depleted plasma with CD4 T cells bound onto poly-L-lysine-coated coverslips for 15 min. Then the supernatant was removed and the cells were washed and incubated for 30 min, with or without PLA2G1B (Figure 8G). pSTAT5 NT was analyzed in CD4 T cells incubated with the adsorbed supernatants.

The effect of the recombinant gp41 and 3S gp41 peptide on PLA2G1B activity was tested by pretreating the cell suspension for 15 min with 40 µl of the recombinant gp41 protein, peptides, with subsequent addition of 10 µl PLA2G1B for 30 min (Figure 8, H-K). The regulation of

PLA2G1B by endogenous gp41 was tested by treating the cell suspension for 30 min with 50 µl of plasma dilutions or 10-30 kDa plasma fraction, previously depleted or not of gp41 (Figures 8, L and M). pSTAT5 NT inhibition was examined by microscopy as described above.

Additional reagents and procedures are detailed in the online Supplemental Material, which includes information on study design and human sample collection, recombinant proteins and peptides, cell purification and culture, detergent-resistant microdomain (DRMs) analysis, western-blot analyses, analysis of the IL-7 receptor (IL-7R) diffusion rate at the surface of living CD4 T lymphocytes, the study of the effect of cytoskeleton inhibitors on pSTAT5 NT, analysis of cytoskeleton organization, identification of PLA2G1B as the active component in VP plasma, active human PLA2G1B structure determination, lipidomic analysis, ELISA, quantitative real-time PCR, immunodepletion experiments, flow cytometry analyses, *in vitro* experiments on mouse T cells, and *in vivo* experiments in mice.

Statistics

Statistical parameters, including the exact value of n, precise measures (mean ± SD in all Figures, with the exception of the mean ± SEM in Figure 7, B-G), statistical significance, and tests used for each analysis are reported in the figures and figure legends. Analyses were performed using GraphPad Prism (GraphPad Software Inc.).
For experiments on human cells, one donor represents one experiment. For experiments on mice, the number of pooled mice from n independent experiments is shown.

Correlations between two variables were evaluated by Pearson's correlation and linear regression.

Data were analyzed using the two-tailed unpaired *t*-test for two groups or ANOVA with correction for multiple comparisons (Tukey's, Dunnett's, or Sidak's) when the distribution was gaussian according to the D'Agostino & Pearson omnibus test. The effect of PLA2G1B on the survival of mouse CD4 T cells in G0 to G5 was analyzed by two-way ANOVA with Dunnett's correction for multiple comparisons using the control condition as the control group. The anti-PLA2G1B effect on CD25 expression and the survival of PLA2G1B-treated mouse CD4 T cells, as well as the kinetics of the effect of PLA2G1B injection on the percentage of cells showing pSTAT5-NT, were analyzed by two-way ANOVA with Sidak's correction for multiple comparisons. When data were not Gaussian, Mann-Whitney's non parametric test was used to compare two groups and Kruskal-Wallis test was used when more than two groups were compared. When Kruskal-Wallis test was significant, two-by-two comparisons were conducted to identify groups which differed, but applying a Bonferroni correction. The level of significance is indicated as $^{*}p < 0.05$, $^{**}p < 0.01$, and $^{***}p < 0.001$ in all figures.

Study approval

Human study: This study was supported by the ANRS and approved by the Comité des Personnes Ile-de-France VII under number 05-15. All participants were adults and provided written informed consent prior to inclusion in the study.

Animal studies: All animal experiments described in the present study were conducted at the Institut Pasteur according to European Union guidelines for the handling of laboratory animals (http://ec.europa.eu/environment/chemicals/lab_animals/home_en.htm) and were approved by the Institut Pasteur Animal Care and Use Committee (CETEA 89, Institut Pasteur de Paris) and the Direction Sanitaire et Vétérinaire de Paris under permit number 2016-0004 and APAFIS#6453-2016071912038344 v2. All experiments were subject to the three R's of animal welfare (refine, reduce, and replace).

AUTHOR CONTRIBUTIONS

J.P., T.R., and F.B. designed and conducted the experiments on human and mouse cells. The study was initiated by T.R and continued by J.P, who participated in the writing of the manuscript. D.G. performed the TCS SPS STED analysis. T.R. designed and conducted the plasma chromatography, biochemical analysis, microscopy image analysis, MS, and bioinformatics data analysis. L.J. participated in the mAb characterization, ELISA development, and recombinant protein production. A.M. participated in the characterization of anti-gp41 mAb. A.H. and F.S. designed and conducted the structural analysis. J.A. and E.R.-M. participated in the studies of plasma from HIV-infected patients. L.T. provided PLA2G1B protein. G.L. contributed to the design of certain experiments, provided ideas and models, and shared resources. J.T. was the lead senior author for this paper.

ACKNOWLEDGMENTS

This work was part of the ANRS programs EP20, EP33, and EP36 (J.-F. Delfraissy, O. Lambotte). It was initially supported by the Institut Pasteur (PTR 424) and the Pasteur-Weizmann Foundation. We are grateful to P. Pouletty for continuous interest and support. We wish to thank U. Schwarz (*Leica Microsystems, Mannheim*), E. Perret, P. Roux, A. Salles, and S. Shorte (*Imagopole, Institut Pasteur*) for their microscopy expertise, as well as A.-H. Pillet for her expertise in biochemistry and P. Bochet for data processing. We thank Yoann Madec and Fredj Tekaia for their help and expertise in statistics. We acknowledge SOLEIL for the provision of synchrotron radiation facilities and thank the staff of the PROXIMA-1 beamline for their assistance. We benefited greatly from help and numerous discussions with C. Abrial, L. Touqui, B. Colsch, D. Troisvallet, M.-L. Gougeon, P. Bruhns, and J. Tiollier. We also gratefully acknowledge J.-P. Routy and B. Malissen for their critical review of the manuscript.

652 **REFERENCES**

653 1. Walker B, McMichael A. The T-cell response to HIV. *Cold Spring Harb Perspect Med.*
654 2012;2(11):a007054.

655 2. Klatt NR, Chomont N, Douek DC, Deeks SG. Immune activation and HIV persistence:
656 implications for curative approaches to HIV infection. *Immunol Rev.* 2013;254(1):326–342.

657 3. Pitman MC, Lau JSY, McMahon JH, Lewin SR. Barriers and strategies to achieve a cure for
658 HIV. *Lancet HIV.* 2018;5(6):e317–e328.

659 4. Doitsh G, et al. Cell death by pyroptosis drives CD4 T-cell depletion in HIV-1 infection.
660 *Nature.* 2014;505(7484):509–514.

661 5. Doitsh G, Greene WC. Dissecting How CD4 T Cells Are Lost during HIV Infection. *Cell*
662 *Host Microbe.* 2016;19(3):280–291.

663 6. Deeks SG, Tracy R, Douek DC. Systemic effects of inflammation on health during chronic
664 HIV infection. *Immunity.* 2013;39(4):633–645.

665 7. de Armas LR, et al. Reevaluation of immune activation in the era of cART and an aging
666 HIV-infected population. *JCI insight.* 2017;2(20):e95726.

667 8. Sousa AE, Carneiro J, Meier-Schellersheim M, Grossman Z, Victorino RMM. CD4 T cell
668 depletion is linked directly to immune activation in the pathogenesis of HIV-1 and HIV-2 but
669 only indirectly to the viral load. *J Immunol.* 2002;169(6):3400–3406.

670 9. George V, et al. Associations of Plasma Cytokine and Microbial Translocation Biomarkers
671 With Immune Reconstitution Inflammatory Syndrome. *J Infect Dis.* 2017;216(9):1159–1163.

672 10. Tincati C, Douek DC, Marchetti G. Gut barrier structure, mucosal immunity and intestinal
673 microbiota in the pathogenesis and treatment of HIV infection. *AIDS Res Ther.* 2016;13(1):19.

674 11. Brenchley JM, et al. Microbial translocation is a cause of systemic immune activation in
675 chronic HIV infection. *Nat Med.* 2006;12(12):1365–1371.

676 12. Hocini H, et al. HIV Controllers Have Low Inflammation Associated with a Strong HIV-

677 Specific Immune Response in Blood. *J Virol.* 2019;93(10):e01690-18.
678 13. Palmer BE, Blyveis N, Fontenot AP, Wilson CC. Functional and phenotypic
679 characterization of CD57+CD4+ T cells and their association with HIV-1-induced T cell
680 dysfunction. *J Immunol.* 2005;175(12):8415–8423.
681 14. Harari A, Petitpierre S, Vallelian F, Pantaleo G. Skewed representation of functionally
682 distinct populations of virus-specific CD4 T cells in HIV-1–infected subjects with progressive
683 disease: changes after antiretroviral therapy. *Blood.* 2004;103(3):966–972.
684 15. Clerici M, et al. Detection of three distinct patterns of T helper cell dysfunction in
685 asymptomatic, human immunodeficiency virus-seropositive patients. Independence of CD4+
686 cell numbers and clinical staging. *J Clin Invest.* 1989;84(6):1892–1899.
687 16. Boswell KL, et al. Loss of Circulating CD4 T Cells with B Cell Helper Function during
688 Chronic HIV Infection. *PLoS Pathog.* 2014;10(1):e1003853.
689 17. Pallikkuth S, de Armas L, Rinaldi S, Pahwa S. T Follicular Helper Cells and B Cell
690 Dysfunction in Aging and HIV-1 Infection. *Front Immunol.* 2017;8:1380.
691 18. Jiang W, et al. Cycling Memory CD4+ T Cells in HIV Disease Have a Diverse T Cell
692 Receptor Repertoire and a Phenotype Consistent with Bystander Activation. *J Virol.*
693 2014;88(10):5369–5380.
694 19. Sieg SF, Bazdar DA, Harding C V, Lederman MM. Differential expression of interleukin-
695 2 and gamma interferon in human immunodeficiency virus disease. *J Virol.* 2001;75(20):9983–
696 9985.
697 20. David D, et al. Regulatory dysfunction of the interleukin-2 receptor during HIV infection
698 and the impact of triple combination therapy. *Proc Natl Acad Sci U S A.* 1998;95(19):11348–
699 11353.
700 21. Colle JH, Moreau JL, Fontanet A, Lambotte O, Delfraissy JF, Thèze J. The correlation
701 between levels of IL-7Ralpha expression and responsiveness to IL-7 is lost in CD4 lymphocytes

from HIV-infected patients. *AIDS.* 2007;21(1):101–103.

22. Colle JH, et al. Regulatory dysfunction of the interleukin-7 receptor in CD4 and CD8 lymphocytes from HIV-infected patients--effects of antiretroviral therapy. *J Acquir Immune Defic Syndr.* 2006;42(3):277–285.

23. Landires I, et al. HIV infection perturbs interleukin-7 signaling at the step of STAT5 nuclear relocalization. *AIDS.* 2011;25(15):1843–1853.

24. Juffroy O, et al. Dual Mechanism of Impairment of Interleukin-7 (IL-7) Responses in Human Immunodeficiency Virus Infection: Decreased IL-7 Binding and Abnormal Activation of the JAK/STAT5 Pathway. *J Virol.* 2010;84(1):96–108.

25. Villarino AV, Kanno Y, O'Shea JJ. Mechanisms and consequences of Jak–STAT signaling in the immune system. *Nat Immunol.* 2017;18(4):374–384.

26. Lin JX, Leonard WJ. The Common Cytokine Receptor γ Chain Family of Cytokines. *Cold Spring Harb Perspect Biol.* 2018;10(9):a028449.

27. Freeman ML, Shive CL, Nguyen TP, Younes SA, Panigrahi S, Lederman MM. Cytokines and T-Cell Homeostasis in HIV Infection. *J Infect Dis.* 2016;214(suppl 2):S51–S57.

28. McLaughlin D, Faller E, Sugden S, MacPherson P. Expression of the IL-7 Receptor Alpha-Chain Is Down Regulated on the Surface of CD4 T-Cells by the HIV-1 Tat Protein. *PLoS One.* 2014;9(10):e111193.

29. Micci L, et al. Paucity of IL-21-producing CD4(+) T cells is associated with Th17 cell depletion in SIV infection of rhesus macaques. *Blood.* 2012;120(19):3925–3935.

30. Shive CL, et al. Inflammatory Cytokines Drive CD4+ T-Cell Cycling and Impaired Responsiveness to Interleukin 7: Implications for Immune Failure in HIV Disease. *J Infect Dis.* 2014;210(4):619–629.

31. Willig KI, Rizzoli SO, Westphal V, Jahn R, Hell SW. STED microscopy reveals that synaptotagmin remains clustered after synaptic vesicle exocytosis. *Nature.*

2006;440(7086):935–939.

32. Dinic J, Riehl A, Adler J, Parmryd I. The T cell receptor resides in ordered plasma membrane nanodomains that aggregate upon patching of the receptor. *Sci Rep.* 2015;5(1):10082.

33. Brownlie RJ, Zamoyska R. T cell receptor signalling networks: branched, diversified and bounded. *Nat Rev Immunol.* 2013;13(4):257–269.

34. Tamarit B, et al. Membrane microdomains and cytoskeleton organization shape and regulate the IL-7 receptor signalosome in human CD4 T-cells. *J Biol Chem.* 2013;288(12):8691–8701.

35. Lambeau G, Gelb MH. Biochemistry and physiology of mammalian secreted phospholipases A2. *Annu Rev Biochem.* 2008;77(1):495–520.

36. Goulder P, Deeks SG. HIV control: Is getting there the same as staying there? *PLoS Pathog.* 2018;14(11):e1007222.

37. Thèze J, Chakrabarti LA, Vingert B, Porichis F, Kaufmann DE. HIV controllers: a multifactorial phenotype of spontaneous viral suppression. *Clin Immunol.* 2011;141(1):15–30.

38. Xu W, Yi L, Feng Y, Chen L, Liu J. Structural insight into the activation mechanism of human pancreatic prophospholipase A2. *J Biol Chem.* 2009;284(24):16659–16666.

39. Janssen MJ, et al. Catalytic role of the active site histidine of porcine pancreatic phospholipase A2 probed by the variants H48Q, H48N and H48K. *Protein Eng.* 1999;12(6):497–503.

40. Blouin CM, Lamaze C. Interferon gamma receptor: the beginning of the journey. [Internet]. *Front Immunol.* 2013;4:267.

41. Marchetti M, et al. Stat-mediated signaling induced by type I and type II interferons (IFNs) is differentially controlled through lipid microdomain association and clathrin-dependent endocytosis of IFN receptors. *Mol Biol Cell.* 2006;17(7):2896–2909.

42. Mercier F, et al. Persistent human immunodeficiency virus-1 antigenaemia affects the

752 expression of interleukin-7Rα on central and effector memory CD4 + and CD8+ T cell subsets.
753 *Clin Exp Immunol.* 2008;152(1):72–80.
754 43. Xu W, et al. CD127 expression in naive and memory T cells in HIV patients who have
755 undergone long-term HAART. *Lab Med.* 2017;48(1):57–64.
756 44. Booth NJ, et al. Different Proliferative Potential and Migratory Characteristics of Human
757 CD4 + Regulatory T Cells That Express either CD45RA or CD45RO . *J Immunol.*
758 2010;184(8):4317–4326.
759 45. Nagafuku M, et al. CD4 and CD8 T cells require different membrane gangliosides for
760 activation. *Proc Natl Acad Sci U S A.* 2012;109(6):E336–E342.
761 46. Vieillard V, Strominger JL, Debré P. NK cytotoxicity against CD4+ T cells during HIV-1
762 infection: a gp41 peptide induces the expression of an NKp44 ligand. *Proc Natl Acad Sci U S*
763 *A.* 2005;102(31):10981–10986.
764 47. Fausther-Bovendo PH, Vieillard V, Sagan S, Bismuth G, Debré P. Hiv gp41 engages gc1qr
765 on cd4+ t cells to induce the expression of an nk ligand through the pip3/h2o2. *PLoS Pathog.*
766 2010;6(7):1–14.
767 48. Pednekar L, et al. Identification of the gC1qR sites for the HIV-1 viral envelope protein
768 gp41 and the HCV core protein: Implications in viral-specific pathogenesis and therapy. *Mol*
769 *Immunol.* 2016;74:18–26.
770 49. Brueseke TJ, Bell JD. A new hat for an old enzyme: Waste management. *Biochim Biophys*
771 *Acta Mol Cell Biol Lipids.* 2006;1761(11):1270-1279.
772 50. Novy P, Quigley M, Huang X, Yang Y. CD4 T cells are required for CD8 T cell survival
773 during both primary and memory recall responses. *J Immunol.* 2007;179(12):8243–8251.
774 51. Becknell B, Caligiuri MA. Interleukin-2, Interleukin-15, and Their Roles in Human Natural
775 Killer Cells. *Adv Immunol.* 2005;86:209–239.
776 52. Pickard JM, Zeng MY, Caruso R, Núñez G. Gut microbiota: Role in pathogen colonization,

immune responses, and inflammatory disease. *Immunol Rev.* 2017;279(1):70–89.

53. Carrette F, Surh CD. IL-7 signaling and CD127 receptor regulation in the control of T cell homeostasis. *Semin Immunol.* 2012;24(3):209-217.

54. Kittipatarin C, Khaled AR. Interlinking interleukin-7. *Cytokine*. 2007;39(1):75-83.

55. Davenport MP, Khoury DS, Cromer D, Lewin SR, Kelleher AD, Kent SJ. Functional cure of HIV: the scale of the challenge. *Nat Rev Immunol.* 2019 Jan;19(1):45-54.

56. Deeks SG, et al. International AIDS Society global scientific strategy: towards an HIV cure 2016. *Nat Med.* 2016;22(8):839–850.

57. Lederman MM, et al. A Cure for HIV Infection: "Not in My Lifetime" or "Just Around the Corner"? *Pathog Immun.* 2016;1(1):154-164.

58. Hell SW, Wichmann J. Breaking the diffraction resolution limit by stimulated emission: stimulated-emission-depletion fluorescence microscopy. *Opt Lett.* 1994;19(11):780–782.

59. Dittami GM, Sethi M, Rabbitt RD, Ayliffe HE. Determination of mammalian cell counts, cell size and cell health using the Moxi Z mini automated cell counter. *J Vis Exp.* 2012;(64):e3842

FIGURE LEGENDS

Figure 1. Characterization of Bumpy T cells from HIV-infected patients.

(**A**) MMD analysis by CW-STED microscopy. From top to bottom, purified HD CD4 T cells (HDc) and VP CD4 T cells (VPc). For each group, the top half of a representative non-stimulated (NS) CD4 T cell, or after IL-7 stimulation, is shown from Z-stack images. (**B**) Quantification of MMDs on the surface of HD CD4 cells (HDc) and VP CD4 cells (VPc) before (NS) and after IL-7 stimulation. (**C**) Size of MMDs at the surface of IL-7-stimulated HD cells (HDc:IL-7) and VP cells before stimulation (VPc:NS). Lines represent the mean values. (**D**) Analysis of IL-7-induced phosphorylation and nuclear translocation of STAT5 by pulsed-STED microscopy (0.5µm slices) in non-stimulated and IL-7-stimulated HD CD4 T cells (top) or VP CD4 T cells (bottom). (**A**-**D**) An average of 50 cells from each HD and 15-50 cells from each VP (HIV RNA/ml = 49,144 ± 33,689) were examined from five donors in each group and representative images are shown in **A** and **D**. (**E**) The kinetics of pSTAT5 in the nucleus (Nuc) and cytoplasm (Cyto) of HD and VP CD4 T cells after IL-7 stimulation was measured using ImageJ and represented as the mean ± SD for three donors.

Figure 2. Analysis of membrane domains and IL-7R distribution on the surface of HD and VP CD4 T cells.

(**A**) Purified CD4 T lymphocytes were lysed (0.5% Triton X-100) and the lysates loaded onto a 5-40% sucrose gradient. After 16 h of centrifugation (50k rpm) at 4°C, 18 fractions were collected (#1 left=tube top=5% sucrose; #18 right=tube bottom=40% sucrose). Each fraction was analyzed by SDS-PAGE (2 gels). Flotillin-1 was used as a marker to indicate low-density fractions corresponding to DRM. IL-7R α and γ chains were revealed by western blotting. Results are shown for purified non-stimulated HD CD4 T-cells (HDc:NS), IL-7-stimulated HD

CD4 T cells (HDc:IL-7), or HD CD4 T-cells pre-treated with cholesterol oxidase (Coase: 31 µM, 25 min) and sphingomyelinase (SMase: 2.7 µM, 5 min), and IL-7-stimulated (HDc:Coase+SMase/IL-7), as well as non-stimulated VP CD4 T cells (VPc:NS) (n=3 donors). (**B**) IL-7Rα chain localization at the membrane of CD4 T cells from HDs and VPs was analyzed by CW-STED. Images of a section (slice) and the top view (top) of representative cells are shown among 50 cells per donor for HD (n=3 donors) and 15-50 cells for VP CD4 T cells (n=3 donors). (**C, D**) The effect of cytoskeletal reorganization and MMD inhibition on IL-7R compartmentalization was evaluated by measuring the two-dimensional effective diffusion rates (D_{eff}) of the IL-7Rα chain by fluorescence correlation spectroscopy (FCS), as described in Tamarit et al., 2013. Histograms represent the effective diffusion rate D_{eff} in each condition at the surface of (**C**) HD (n=3 donors) and (**D**) VP CD4 T cells (n=3 donors).

Figure 3. Induction of Bumpy CD4 T cells by plasma from HIV-infected patients.

(**A**) CW-STED images of MMDs on HD CD4 T cells treated with 10% HDp (HDc:HDp) or VPp (HDc:VPp) before and after IL-7 stimulation. (**B**) Dose-effect of plasma from HD (HDp, n=5), VP (VPp, n=5, HIV RNA/ml = 49,144 ± 33,689), HIV-controllers (HICp, n=3), and ART-treated donors (ARTp, n=3) on the number of MMDs per HD CD4 T cell. (**C**) Pulsed-STED images of pSTAT5 of HD CD4 T cells pre-treated with 10% plasma from HDs or VPs. (**D**) Plasma dose-effects as in **B** on pSTAT5 NT in IL-7-treated HD CD4 T cells. Data are represented as the mean ± SD. (**A-D**) For each condition, an average of 50 HD CD4 T cells were analyzed from five donors and representative images are shown in **A** and **C**. (**E**) Pearson's correlation between the kinetics of pSTAT5 NT and the number of physiological MMDs throughout IL-7 activation of HD cells (up to 60 min). Linear regression for the mean of the five HD plasma samples is shown. (**F**) Pearson's correlation between pSTAT5 NT and abnormal MMDs per HD CD4 T cell treated with various amounts of plasma from HD (HDp,

n=5), VP (VPp, n=5, HIV RNA/ml = 49,144 ± 33,689), HIV-controllers (HICp, n=3), and ART-treated donors (ARTp, n=3). Linear regression for the mean of the five VP plasma samples is shown.

Figure 4. Cloned plasma PLA2G1B induces the Bumpy T-cell phenotype.

(**A**) Crystal structure of PLA2G1B. (**B**) PLA2G1B effect on MMD formation followed by STED (representative of two experiments at 250 nM and verified at 500 nM and 1µM). (**C**) Dose-effect of PLA2G1B on IL-7-induced pSTAT5 NT in HD purified CD4 T cells after analysis of confocal images. Results are shown as the mean ± SD from four donors. (**D-G**) The effects on aMMD formation (**D**, **E**) and pSTAT5 NT (**F**, **G**) in CD4 T cells of 250 nM wildtype PLA2G1B were compared to those of the non-active mutant H48Q (**D**, **F**) and other PLA2s (PLA2GIIA, PLA2GIID, or PLA2GX, **E**, **G**). Results are shown as the mean ± SD from five (**D-F**) or seven donors (**G**). (**H**) VP plasma (3%, from 5 donors) was depleted with anti-PLA2G1B, anti-PLA2GIIA or anti-PLA2GIID rabbit polyclonal antibodies (100 µg/mL). The effect of depletion was analyzed by following pSTAT5 NT in IL-7-stimulated-CD4 T cells (n=3 donors) incubated with depleted plasma. Results were normalized to the response obtained with HD plasma and are shown as the mean ± SD. (**I**) Effect of VPp treated with various doses of neutralizing anti-PLA2G1B mAb 14G9 on pSTAT5 NT in CD4 T cells from one donor and the effect of 100 µg/mL of 14G9 mAb on pSTAT5 NT in CD4 T cells from five donors. $^{*}p<0.05$, $^{**}p<0.01$ and $^{***}p<0.001$ by the Mann-Whitney *t*-test (**D**, **F**, **I**) and by the Kruskal-Wallis test followed by the Mann-Whitney test with p-values adjusted for multiple comparisons between groups (**E**, **G**) or one-way ANOVA (**H**) with Tukey's correction for multiple comparisons.

Figure 5. Effect of PLA2G1B on CD4 T-cell subpopulations, specificity, and reversion.

(**A**) Dose-effect of PLA2G1B (IL-7: n=4, IL-2: n=3 and IL-4: n=5) and (**B**) of 1% HDp (IL-7: n=4, IL-2 and IL-4: n=3) and VPp (n=5) on IL-2, IL-4, and IL-7-induced pSTAT translocation in CD4 T cells. (**C**) Effects of PLA2G1B (IL-7: n=4, IFN-α: n=5) and **(D**) plasma (HD (n=4) or VP (n=5), 1%) on IL-7-induced pSTAT5 NT and IFN-α-induced pSTAT1 NT in CD4 T cells (n = 5 donors). (**E**) The effect of PLA2G1B (30 min) on IL-7-induced pSTAT5 NT was analyzed in total (HD T CD4+:IL-7), naïve (HD T CD4+ CD45RA+:IL-7), and memory (HD T CD4+ CD45RA-:IL-7) CD4 T cells from the same donor in response to IL-7 (n=3 donors). (**F**) Percentage of CD127+ cells among and (**G**) CD127 expression (delta anti-CD127 MFI minus isotype control MFI) on CD45RA+ and CD45RA- CD4 T cells after treatment with 1µM WT or H48Q PLA2G1B (see gating strategy in Supplemental Figure 3A, n=3 donors). (**H**) Effect of PLA2G1B (250 nM) on aMMD induction in CD4 T cells (n=5) and CD8 T cells (n=8) and (**I**) on IL-7-induced pSTAT5 NT in CD8 T cells (dose-effect, n=3). (**A-I**) Results are shown as the mean ± SD. $^{*}p<0.05$, $^{**}p<0.01$ and $^{***}p<0.001$ by one-way ANOVA (**B-D)** and two-way ANOVA (**E**) with Tukey's correction for multiple comparisons or $^{**}p<0.01$ by the Mann-Whitney two tailed unpaired *t*-test (**H**). (**J**) Anti-PLA2G1B treatment accelerates the recovery of a functional pSTAT5 NT response of PLA2G1B-treated CD4 T cells to IL-7. The results of one representative experiment of three are presented.

Figure 6. PLA2G1B acts on dying CD4 T cells and reduces CD4 T-cell survival.

(**A**, **B**) PLA2G1B reduces the survival of human CD4 T cells. (**A**) Cells were treated with PBS (Ctrl) or various amounts of PLA2G1B (1, 10, 100 µM) for one experiment. Results are shown as the percentage of CD4 T-cell counts normalized to the number of Ctrl cells at each time point. (**B**) Cells were treated with PBS (Ctrl) or 250 nM PLA2G1B (n=6 donors). Results are shown as the mean ± SD of the percentage of CD4 T-cell counts normalized to the number of

Ctrl cells at each time point. (**A**, **B**) The lines show the linear regression and the p-values indicate the significance of difference with control. (**C**-**E**) PLA2G1B acts on dying CD4 T cells and digests phosphatidylserine. FACS analysis of $CD4^+$ T cells for Annexin V-APC on Live/Dead Marker (Zombie-Violet) positive cells after treatment with (**C**) 250 nM PLA2G1B WT or H48Q or (**D**) 250 nM PLA2G1B with anti-PLA2G1B (14G9) or not (w/o Ab). (**C**, **D**) Annexin V-APC labelling (MFI) at various time points post-treatment are presented (one representative experiment of two in **C** and three in **D** is presented). (**E**) Results are shown as the mean ± SD of the percentage of Annexin V-negative Zombie-positive CD4 T cells after treatment with PBS (Ctrl), PLA2G1B alone (w/o Ab), or anti-PLA2G1B (14G9) (n=3 donors). (**F**) Anti-PLA2G1B treatment inhibits the effect of PLA2G1B on the survival of CD4 T cells. Results are shown as the mean ± SD of the percentage of CD4 T-cell counts normalized to the number of Ctrl cells at each time point (n=3 donors). Lines show the linear regression and p-value indicate the significance difference between experimental conditions, $^{*}p<0.05$, $^{***}p<0.001$.

Figure 7. Immunological effects of hPLA2G1B on mouse CD4 T cells in vitro and in vivo. (**A**-**G**) FACS analysis of the effect of hPLA2G1B on mouse $CD4^+$ T cells after anti-CD3/CD28 and IL-2 stimulation (five days, see gating strategy on Supplemental Figure 6C). (**A**-**E**) $mCD4^+$ T cells were pretreated with WT or H48Q hPLA2G1B. (**A**) CD25 expression after treatment with 125 nM. (**B**) CD25 expression (MFI) and (**C**) cell survival (n=3, 10 mice). (**D**) $mCD4^+$ T-cell proliferation profile after treatment with 125 nM. (**E**) Percentage of live $mCD4^+$ T cells per cell generation (Go to G5; n=3, 9 mice). (**F**, **G**) Effects of mAb anti-PLA2G1B 14G9 in vitro treatment on 125nM hPLA2G1B action on $CD4^+$ T-cell survival and CD25 expression (n=4, 11 mice). (**H**-**L**) In vivo effects of hPLA2G1B on CD4 T-cell response to IL-7. Spleen CD4 T cells were isolated after intraperitoneal injection into C57BL/6 mice and the ex vivo pSTAT5

NT response to IL-7 was evaluated by confocal microscopy with an average of 200 cells examined for each condition. Effect of hPLA2G1B injection at several doses of PLA2G1B for 3 h (6 mice/2 experiments, **H**) and at several times post-injection (3 mice/1 experiment, **I**; 8 mice/2 experiments, **J**). (**K**) Effects of mAb anti-hPLA2G1B 14G9 injected in vivo on the hPLA2G1B (100 µg, 3 h) response (5 mice/1 experiment). (**L**) Inhibition of the effects of hPLA2G1B after injection into hPLA2G1B/BSA-immunized mice (5 mice/1 experiment). Results are shown as the mean ± SEM (**B**, **C** and **E-G**) ± SD (**H-L**). $^{*}p<0.05$, $^{**}p<0.01$ and $^{***}p<0.001$ are adjusted p-value for multiple comparisons performed by Kruskal-Wallis test $p<0.001$, followed by the Mann-Whitney test (**B**) and two-way ANOVA with correction for multiple comparisons of Tukey (**C**, **H, J-L),** Dunnett with the condition w/o PLA2G1B as a control group (**E**), or Sidak (**F**, **G**, **I**).

Figure 8. Synergy between PLA2G1B activity and gp41.

(**A, B**) ELISA quantification of PLA2G1B in plasma from HD, VP, HIV-controllers (HIC) and ART-treated donors (ART) (median is shown). The Kruskal-Wallis test p-value was 0.0025 on A and then multiple comparisons were performed using the Mann-Whitney test. $^{***}p<0.001$. (**C**) Level of *pla2g1b* RNA in PBMCs from HDs and VPs. Results are shown as the mean ± SD of the number of copies of *pla2g1b*/µg of total RNA. (**D**) Inhibitory activity of PLA2G1B diluted in PBS buffer or plasma from HDs or VPs previously depleted (Δ) of endogenous PLA2G1B ($p<0.0001$ non-linear regression in VPp relatively to HDp/buffer). (**E**) The same experiment as in (**D**) with 1% plasma and 5 or 75 nM PLA2G1B. (**F**) VP plasma previously adsorbed on CD4 T cells. Adsorbed plasma or buffer were collected and used to treat other CD4 T cells together with PLA2G1B or not. (**G**) PLA2G1B activity on VP plasma-pretreated CD4 T cells. CD4 T cells were pretreated with plasma or buffer, then plasma or buffer were removed and PLA2G1B was added, or not, to the pretreated CD4 T cells. (**H**, **I**) PLA2G1B

inhibitory activity in the presence of the gp41 fragment (**J**, **K**) or 3S or control (CTL) peptides. (**L, M**) Inhibitory activity of 1% or 3% VP plasma depleted with anti-gp41 (gp41) polyclonal antibody (pAb) (**L**) or anti-3S gp41 monoclonal antibody (Anti-3S) (**M**), control (ctrl) or not depleted (w/o Ab) on CD4 T cells. **D**, **H** and **J** show one representative dose-response experiments among 2-3. (**E-G**, **I**, **K-M**) results are shown as the mean ± SD of the percentage of pSTAT5 NT cells inhibition on 3-4 donors, as indicated. $^{*}p<0.05$, $^{**}p<0.01$ by two tailed unpaired *t*-test (**I** and **K**), $^{***}p<0.001$ by ANOVA with Tukey's correction for multiple comparisons (**E-G**, **L** and **M**).

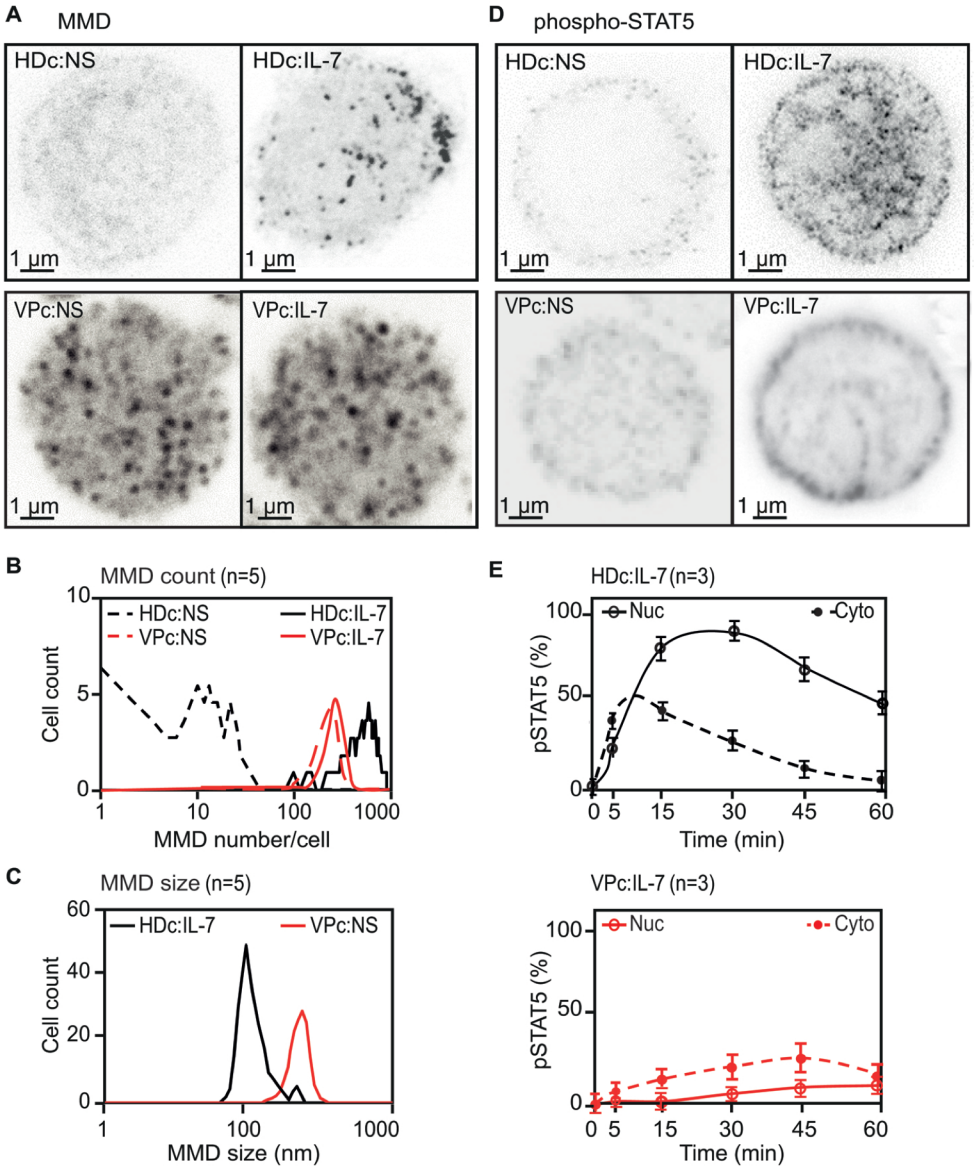

Figure 1. Characterization of Bumpy T cells from HIV-infected patients.
(**A**) MMD analysis by CW-STED microscopy. From top to bottom, purified HD CD4 T cells (HDc) and VP CD4 T cells (VPc). For each group, the top half of a representative non-stimulated (NS) CD4 T cell, or after IL-7 stimulation, is shown from Z-stack images. (**B**) Quantification of MMDs on the surface of HD CD4 cells (HDc) and VP CD4 cells (VPc) before (NS) and after IL-7 stimulation. (**C**) Size of MMDs at the surface of IL-7-stimulated HD cells (HDc:IL-7) and VP cells before stimulation (VPc:NS). Lines represent the mean values. (**D**) Analysis of IL-7-induced phosphorylation and nuclear translocation of STAT5 by pulsed-STED microscopy (0.5µm slices) in non-stimulated and IL-7-stimulated HD CD4 T cells (top) or VP CD4 T cells (bottom). (**A-D**) An average of 50 cells from each HD and 15-50 cells from each VP (HIV RNA/ml = 49,144 ± 33,689) were examined from five donors in each group and representative images are shown in **A** and **D**. (**E**) The kinetic of pSTAT5 in the nucleus (Nuc) and cytoplasm (Cyto) of HD and VP CD4 T cells after IL-7 stimulation was measured using ImageJ and represented as the mean ± SD for three donors.

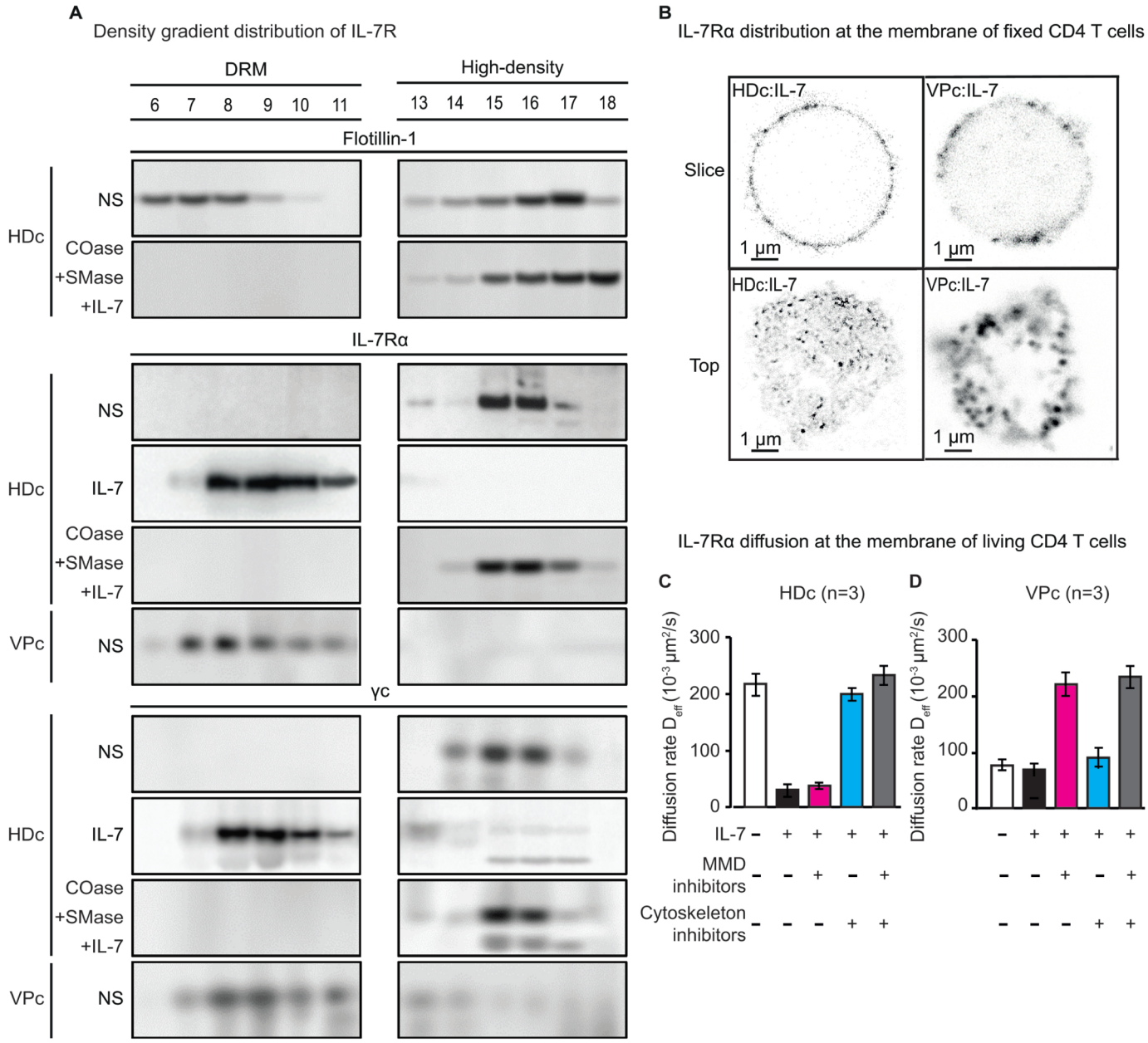

Figure 2. Analysis of membrane domains and IL-7R distribution on the surface of HD and VP CD4 T cells.

(**A**) Purified CD4 T lymphocytes were lysed (0.5% Triton X-100) and the lysates were loaded onto a 5-40% sucrose gradient. After 16 h of centrifugation (50k rpm) at 4°C, 18 fractions were collected (#1 left=tube top=5% sucrose; #18 right=tube bottom=40% sucrose). Each fraction was analyzed by SDS-PAGE (2 gels). Flotillin-1 was used as a marker to indicate low-density fractions corresponding to DRM. IL-7R α and γ chains were revealed by western blotting. Results are shown for purified non-stimulated HD CD4 T-cells (HDc:NS), IL-7-stimulated HD CD4 T cells (HDc:IL-7), or HD CD4 T-cells pre-treated with cholesterol oxidase (Coase: 31 µM, 25 min) and sphingomyelinase (SMase: 2.7 µM, 5 min), and IL-7-stimulated (HDc:Coase+SMase/IL-7), as well as non-stimulated VP CD4 T cells (VPc:NS) (n=3 donors). (**B**) IL-7Rα chain localization at the membrane of CD4 T cells from HDs and VPs was analyzed by CW-STED. Images of a section (slice) and of the top view (top) of representative cells are shown among 50 cells per HD (3 donors) and 15 to 50 cells per VP CD4 T cells (3 donors). (**C, D**) The effect of cytoskeletal reorganization and MMD inhibitions on IL-7R compartmentalization was evaluated by measuring the two-dimensional effective diffusion rates (D_{eff}) of the IL-7Rα chain by fluorescence correlation spectroscopy (FCS) as described in Tamarit et al., 2013. Histograms represent the effective diffusion rate D_{eff} in each condition at the surface of (**C**) HD (3 donors) and (**D**) VP CD4 T cells (3 donors).

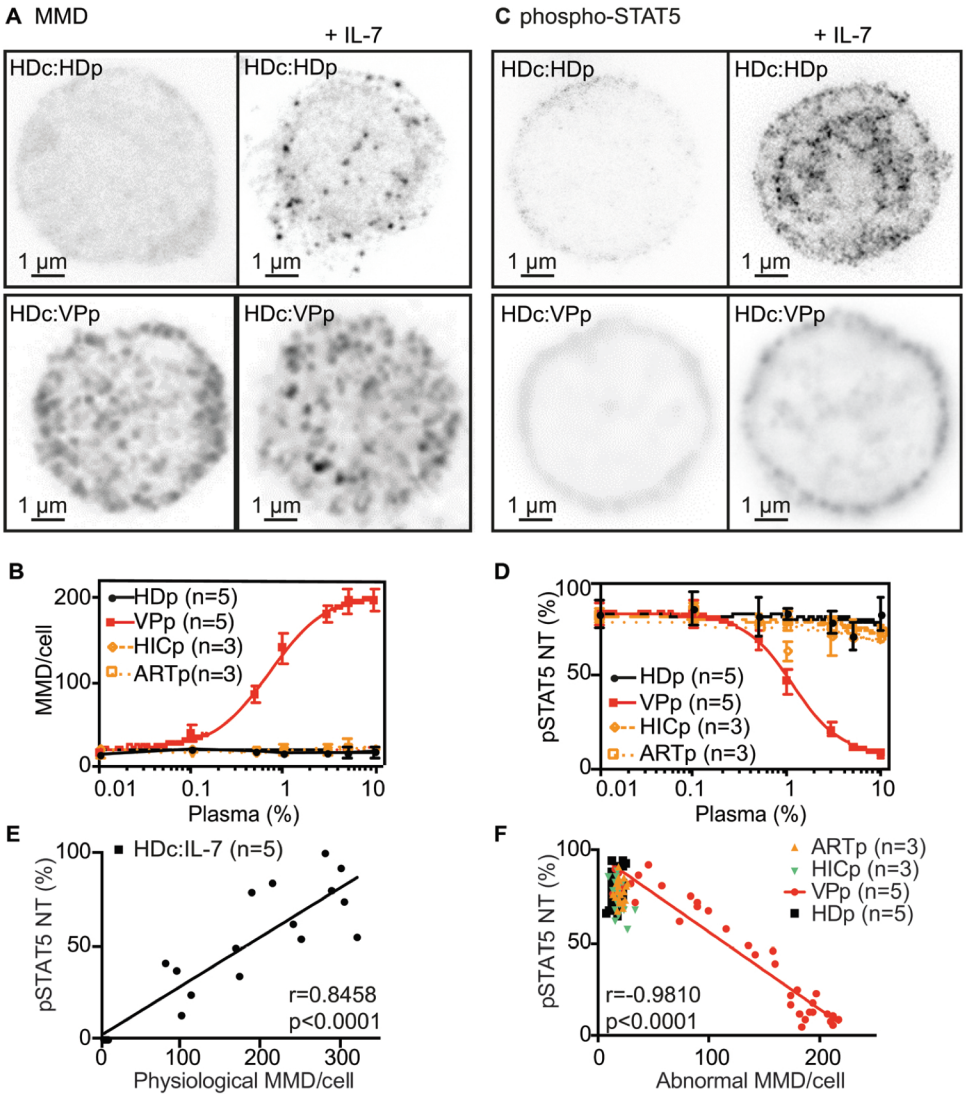

Figure 3. Induction of Bumpy CD4 T cells by plasma from HIV-infected patients. (**A**) CW-STED images of MMD on HD CD4 T cells treated with 10% HDp (HDc:HDp) or VPp (HDc:VPp) before and after IL-7 stimulation. (**B**) Dose-effect of plasmas from HD (HDp, n=5), VP (VPp, n=5, HIV RNA/ml = 49,144 ± 33,689), HIV-controllers (HICp, n=3), and ART-treated donors (ARTp, n=3) on the number of MMDs per HD CD4 T cell. (**C**) Pulsed-STED images of pSTAT5 of HD CD4 T cells pre-treated with 10% plasma from HDs or VPs. (**D**) Plasma dose-effects on pSTAT5 NT in IL-7-treated HD CD4 T cells. Data are represented as the mean ± SD. (**A**-**D**) For each condition, an average of 50 HD CD4 T cells were analyzed from five donors and representative images are shown in **A** and **C**. (**E**) Pearson's correlation between the kinetics of pSTAT5 NT and the number of physiological MMDs throughout IL-7 activation of HD cells (up to 60 min). Linear regression for the mean of the five HD plasma samples is shown. (**F**) Pearson's correlation between pSTAT5 NT and abnormal MMD per HD CD4 T cell treated with various amount of plasma from HD (HDp, n=5), VP (VPp, n=5, HIV RNA/ml = 49,144 ± 33,689), HIV-controllers (HICp, n=3) and ART-treated donors (ARTp, n=3). Linear regression for the mean of the five VP plasma samples is shown.

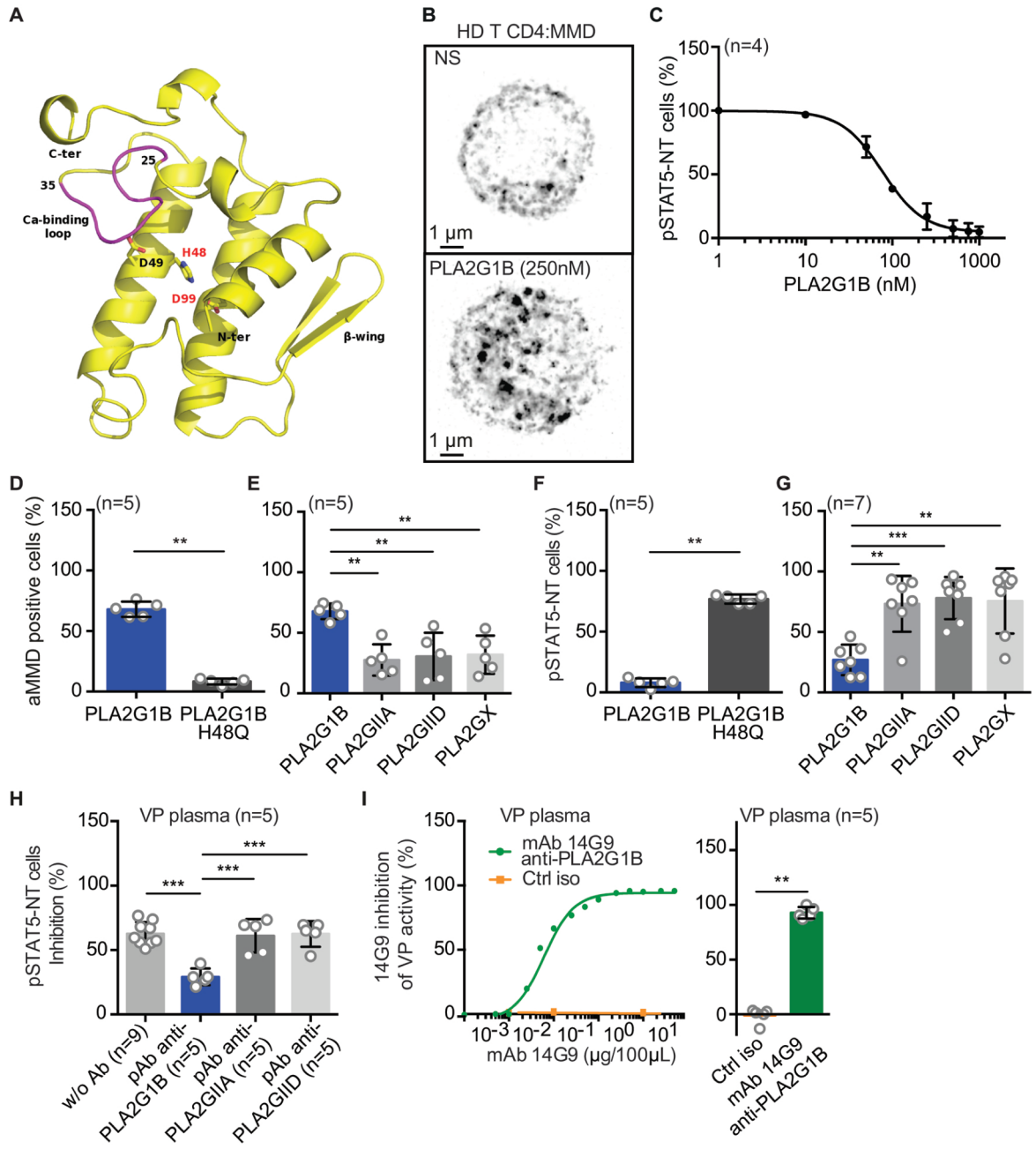

Figure 4. Cloned plasma PLA2G1B induces the Bumpy T-cell phenotype.

(**A**) Crystal structure of PLA2G1B. (**B**) PLA2G1B effect on MMD formation followed by STED (representative of two experiments at 250 nM and verified at 500 nM and 1µM). (**C**) Dose-effect of PLA2G1B on IL-7-induced pSTAT5 NT in HD purified CD4 T cells after analysis of confocal images. Results are shown as the mean ± SD from four donors. (**D-G**) The effects on aMMD formation (**D**, **E**) and pSTAT5 NT (**F**, **G**) in CD4 T cells at 250 nM of wildtype PLA2G1B were compared to those of the non-active mutant H48Q (**D, F**) and of other PLA2s (PLA2GIIA, PLA2GIID, or PLA2GX) (**E**, **G**). Results are shown as the mean ± SD from five (**D-F**) or seven donors (**G**). (**H**) VP plasma (3%, from 5 donors) was depleted with anti-PLA2G1B, anti-PLA2GIIA or anti-PLA2GIID rabbit polyclonal antibodies (100 µg/mL). The effect of depletion was analyzed by following pSTAT5 NT in IL-7-stimulated-CD4 T cells (n=3 donors) incubated with depleted plasma. Results were normalized to the response obtained with HD plasma and are shown as the mean ± SD. (**I**) Effect of VPp treated with various doses of neutralizing anti-PLA2G1BmAb 14G9 on pSTAT5 NT in CD4 T cells from one donor and the effect of 100 µg/mL of 14G9 mAb on pSTAT5 NT in CD4 T cells from five donors. $^{*}p<0.05$, $^{**}p<0.01$ and $^{***}p<0.001$ by the Mann-Whitney *t*-test (**D**, **F**, **I**) and by the Kruskal-Wallis followed by the Mann-Whitney test with p-values adjusted for multiple comparison between groups (**E**, **G**) or one way ANOVA (**H**) with Tukey's correction for multiple comparisons.

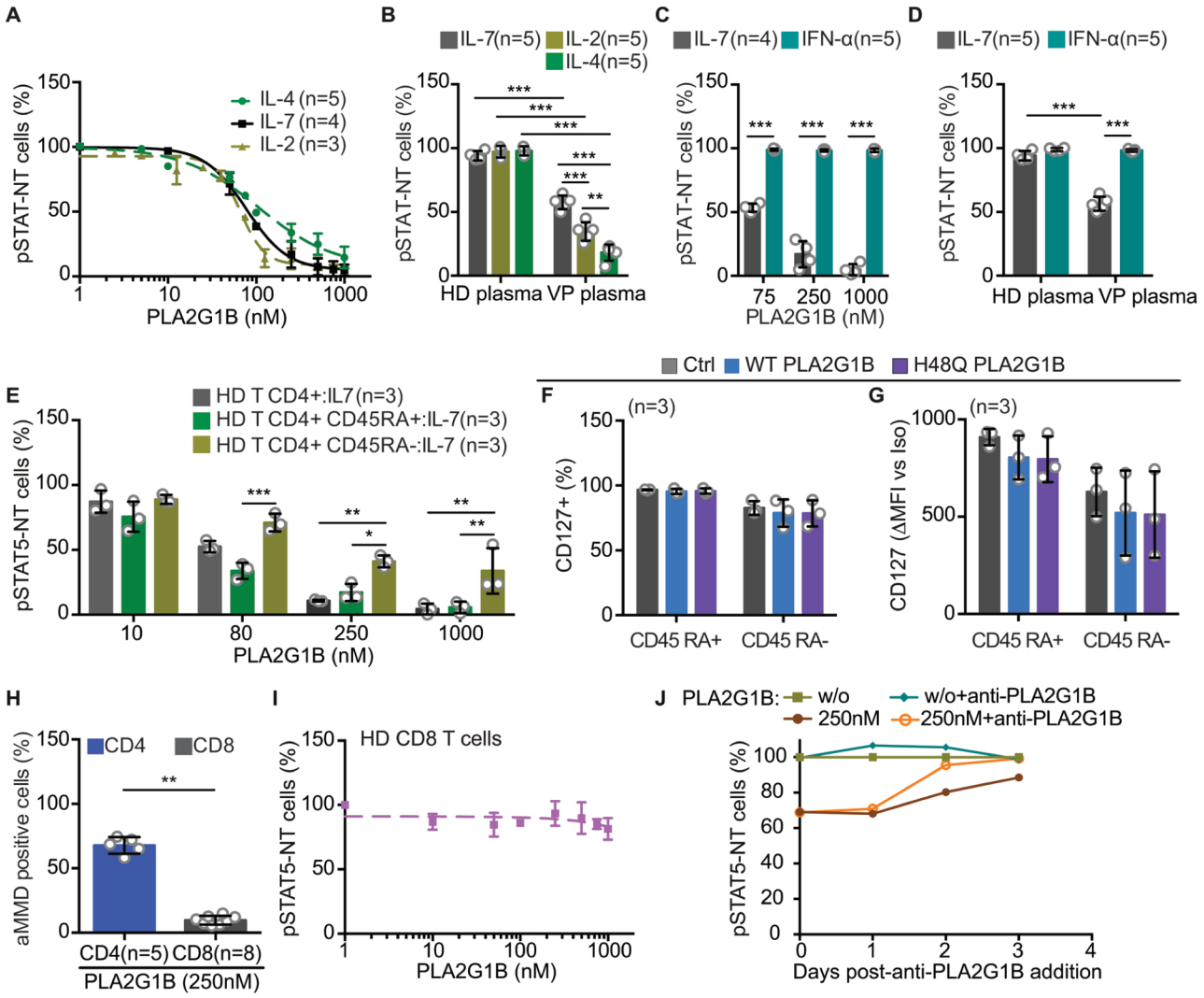

Figure 5. Effect of PLA2G1B on CD4 T-cell subpopulations, specificity, and reversion. (**A**) Dose-effect of PLA2G1B (IL-7: n=4, IL-2: n=3 and IL-4: n=5) and (**B**) of 1% HDp (IL-7: n=4, IL-2 and IL-4: n=3) and VPp (n=5) on IL-2, IL-4, and IL-7-induced pSTAT translocation in CD4 T cells. (**C**) Effects of PLA2G1B (IL-7: n=4, IFN-α: n=5) and (**D**) plasmas (HD (n=4) or VP (n=5), 1%) on IL-7-induced pSTAT5 NT and IFN-α-induced pSTAT1 NT in CD4 T cells (n = 5 donors). (**E**) The effect of PLA2G1B (30 min) on IL-7-induced pSTAT5 NT was analyzed in total (HD T CD4+:IL-7), naïve (HD T CD4+ CD45RA+:IL-7), and memory (HD T CD4+ CD45RA-:IL-7) CD4 T cells from the same donor in response to IL-7 (n=3 donors). (**F**) Percentage of CD127+ cells among and (**G**) CD127 expression (delta anti-CD127 MFI minus isotype control MFI) on CD45RA+ and CD45RA- CD4 T cells after treatment with 1µM WT or H48Q PLA2G1B (see gating strategy in Supplemental Figure 3A, n=3 donors). (**H**) Effect of PLA2G1B (250 nM) on aMMD induction in CD4 T cells (n=5) and CD8 T cells (n=8) and (**I**) on IL-7-induced pSTAT5 NT in CD8 T cells (dose-effect, n=3). (**A-I**) Results are shown as the mean ± SD. $^{*}p<0.05$, $^{**}p<0.01$ and $^{***}p<0.001$ by one way ANOVA (**B-D**) and two way ANOVA (**E**) with Tukey's correction for multiple comparison or $^{**}p<0.01$ by the Mann-Whitney two tailed unpaired *t*-test (**H**). (**J**) Anti-PLA2G1B treatment accelerates the recovery of a functional pSTAT5 NT response of PLA2G1B-treated CD4 T cells to IL-7. The results of one representative of three experiments are presented.

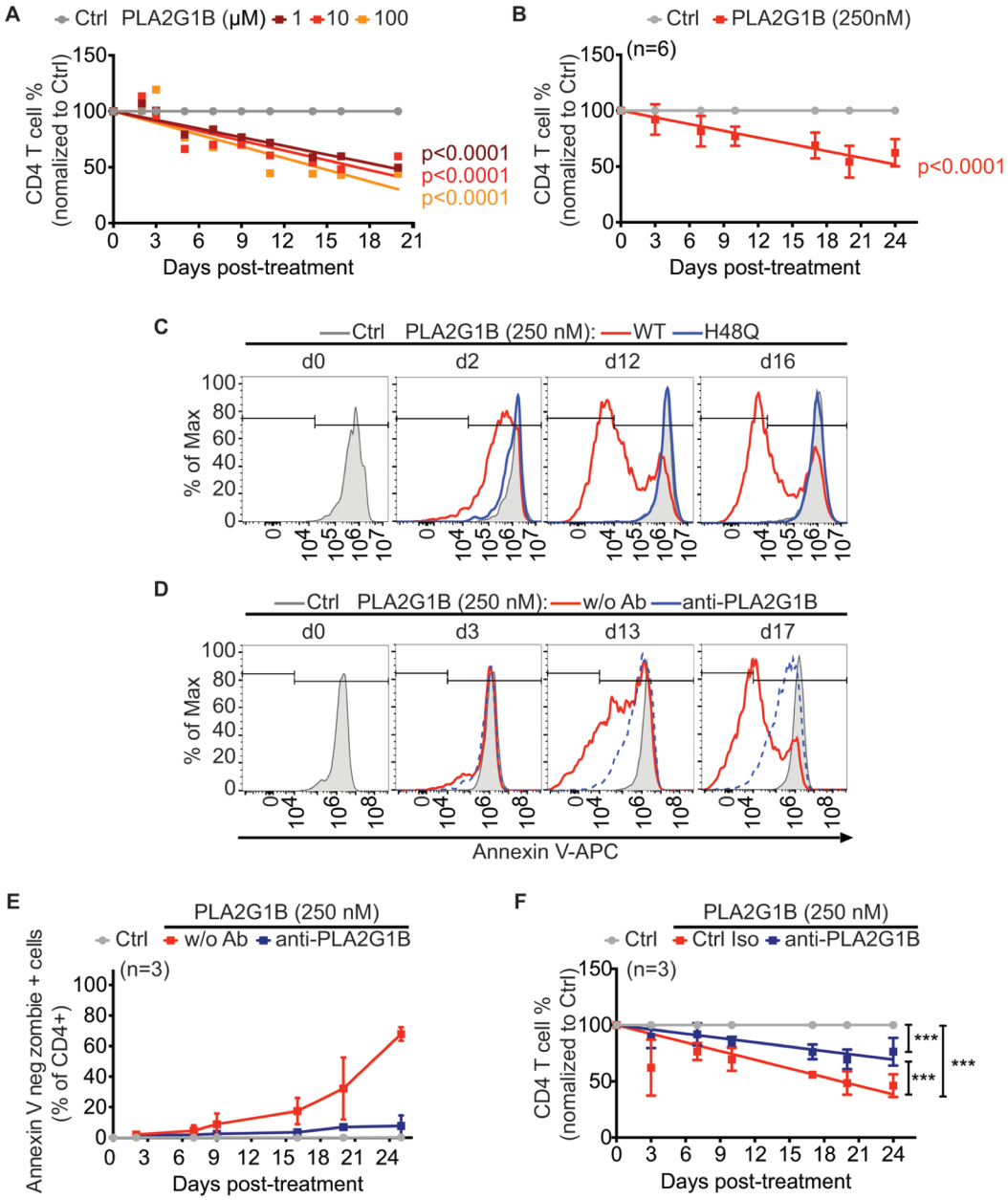

Figure 6. PLA2G1B acts on dying CD4 T cells and reduces CD4 T-cell survival.
(**A, B**) PLA2G1B reduces the survival of human CD4 T cells. (**A**) Cells were treated with PBS (Ctrl) or various amounts of PLA2G1B (1, 10, 100 µM) for one experiment. Results are shown as the percentage of CD4 T-cell counts normalized to the number of Ctrl cells at each time point. (**B**) Cells were treated with PBS (Ctrl) or 250 nM PLA2G1B (n=6 donors). Results are shown as the mean ± SD of the percentage of CD4 T-cell counts normalized to the number of Ctrl cells at each time point. (**A**, **B**) The lines show the linear regression and the p-values indicate the significance of difference with control. (**C**-**E**) PLA2G1B acts on dying CD4 T cells and digests phosphatidylserine. FACS analysis of $CD4^+$ T cells for Annexin V-APC on Live/Dead Marker (Zombie-Violet) positive cells after treatment with (**C**) 250 nM PLA2G1B WT or H48Q or (**D**) 250 nM PLA2G1B with anti-PLA2G1B (14G9) or not (w/o Ab). (**C**, **D**) Annexin V-APC labelling (MFI) at various time points post-treatment are presented (one representative experiments of two in **C** and three in **D** is presented). (**E**) Results are shown as the mean ± SD of the percentage of Annexin V-negative Zombie-positive CD4 T cells after treatment with PBS (Ctrl), PLA2G1B alone (w/o Ab), or with anti-PLA2G1B (14G9) (n=3 donors). (**F**) Anti-PLA2G1B treatment inhibits the effect of PLA2G1B on the survival of CD4 T cells. Results are shown as the mean ± SD of the percentage of CD4 T-cell counts normalized to the number of Ctrl cells at each time point (n=3 donors). Lines show the linear regression and p-value indicate the significance difference between experimental conditions, $^{***}p<0.001$.

Figure 7. Immunological effects of hPLA2G1B on mouse CD4 T cells in vitro and in vivo.

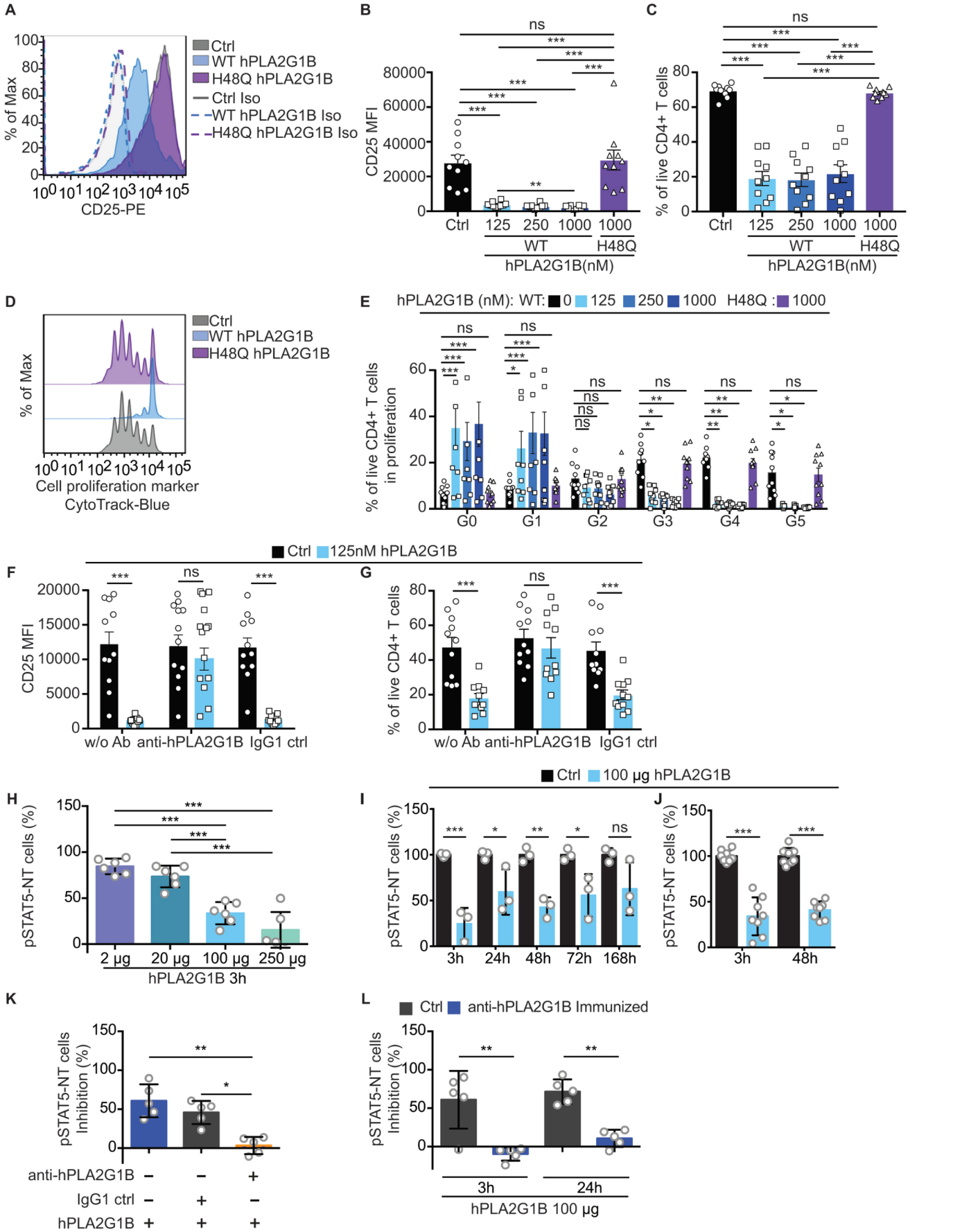

Figure 7. Immunological effects of hPLA2G1B on mouse CD4 T cells in vitro and in vivo. (**A-G**) FACS analysis of the effect of hPLA2G1B on mouse $CD4^+$ T cells after anti-CD3/CD28 and IL-2 stimulation (five days, see gating strategy on Supplemental Figure 6C). (**A-E**) $mCD4^+$ T cells were pretreated with WT or H48Q hPLA2G1B. (**A**) CD25 expression after treatment with 125 nM. (**B**) CD25 expression (MFI) and (**C**) cell survival (n=3, 10 mice). (**D**) $mCD4^+$ T-cell proliferation profile after treatment with 125 nM. (**E**) Percentage of live $mCD4^+$ T cells per cell generation (Go to G5; n=3, 9 mice). (**F**, **G**) Effects of mAb anti-PLA2G1B 14G9 in vitro treatment on 125nM hPLA2G1B action on $CD4^+$ T-cell survival and CD25 expression (n=4, 11 mice). (**H-L**) In vivo effects of hPLA2G1B on CD4 T-cell response to IL-7. Spleen CD4 T cells were isolated after intraperitoneal injection into C57BL/6 mice and the ex vivo pSTAT5 NT response to IL-7 was evaluated by confocal microscopy with an average of 200 cells examined for each condition. Effect of hPLA2G1B injection at several doses of PLA2G1B for 3 h (6 mice/2 experiments, **H**) and at several times post-injection (3 mice/1 experiment, **I**; 8 mice/2 experiments, **J**). (**K**) Effects of mAb anti-hPLA2G1B 14G9 injected in vivo on the hPLA2G1B (100 µg, 3 h) response (5 mice/1 experiment). (**L**) Inhibition of the effects of hPLA2G1B after injection into hPLA2G1B/BSA-immunized mice (5 mice/1 experiment). Results are shown as the mean ± SEM (**B**, **C** and **E-G**) ± SD (**H-L**). $^{*}p<0.05$, $^{**}p<0.01$ and $^{***}p<0.001$ are adjusted p-value for multiple comparisons performed by Kruskal-Wallis test $p<0.001$, followed by the Mann-Whitney test (**B**) and two-way ANOVA with correction for multiple comparisons of Tukey (**C**, **H, J-L**), Dunnett, with the condition w/o PLA2G1B as a control group (**E**), or Sidak (**F**, **G**, **I**).

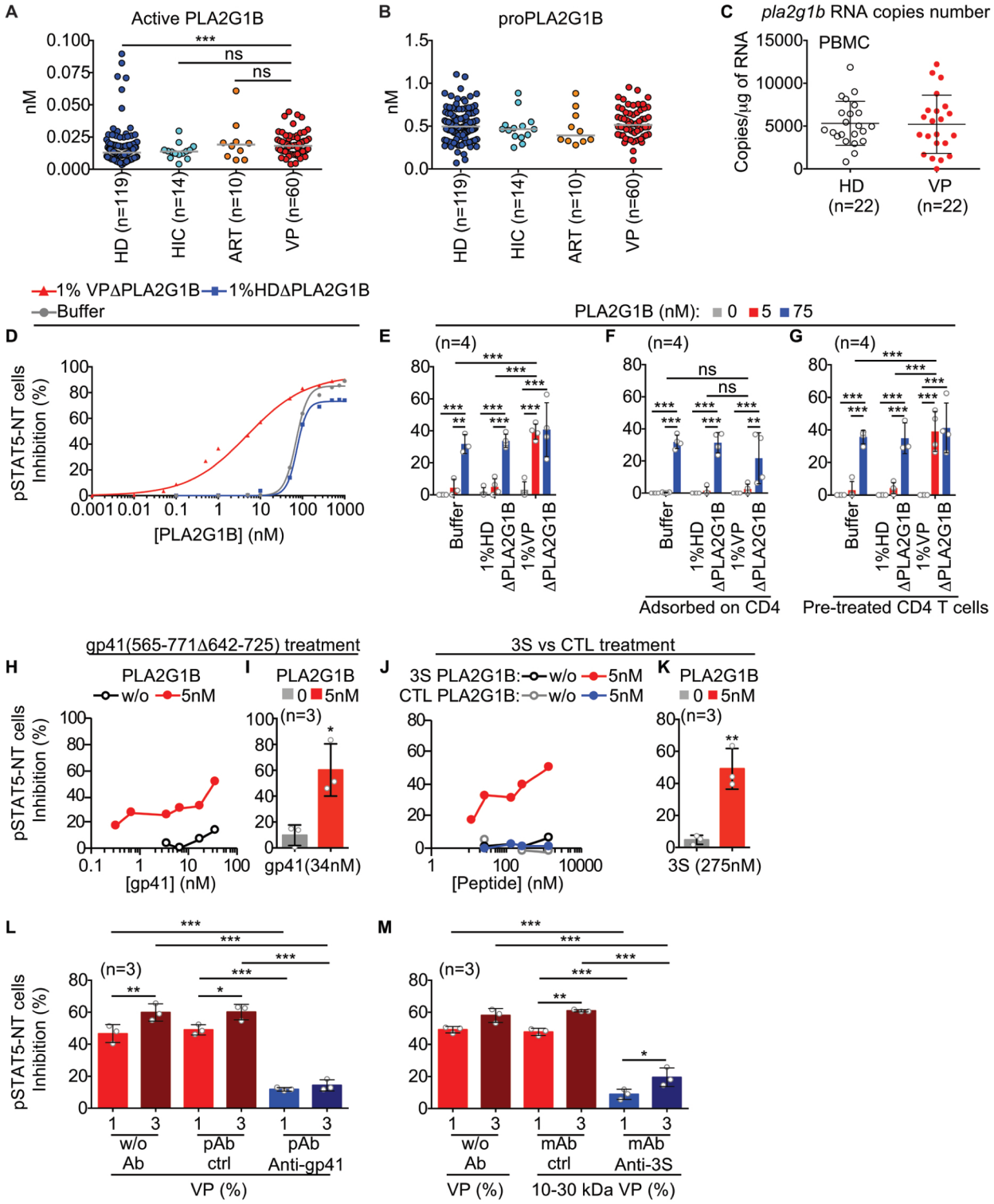

Figure 8. Synergy between PLA2G1B activity and gp41.

(**A, B**) ELISA quantification of PLA2G1B in plasma from HD, VP, HIV-controllers (HIC) and ART-treated donors (ART) (median is shown). The Kruskal-Wallis test p-value was 0.0025 on A and then multiple comparisons were performed using the Mann-Whitney test. $^{***}p<0.001$. (**C**) Level of pla2g1b RNA in PBMCs from HDs and VPs. Results are shown as mean ± SD of the number of copies of pla2g1b/µg of total RNA. (**D**) Inhibitory activity of PLA2G1B diluted in PBS buffer or plasma from HDs or VPs previously depleted (Δ) of endogenous PLA2G1B ($p<0.0001$ non-linear regression in VPp relatively to HDp/buffer). (**E**) The same experiment as in (**D**) with 1% plasma and 5 or 75 nM PLA2G1B. (**F**) VP plasma previously adsorbed on CD4 T cells. Adsorbed plasma or buffer were collected and used to treat other CD4 T cells together with PLA2G1B or not. (**G**) PLA2G1B activity on VP plasma-pretreated CD4 T cells. CD4 T cells were pretreated with plasma or buffer, then plasma or buffer were removed and PLA2G1B was added, or not, to the pretreated CD4 T cells. (**H**, **I**) PLA2G1B inhibitory activity in the presence of the gp41 fragment (**J**, **K**) or 3S or control (CTL) peptides. (**L, M**) Inhibitory activity of 1% or 3% VP plasma depleted with anti-gp41 (gp41) polyclonal antibody (pAb) (**L**) or anti-3S gp41 monoclonal antibody (Anti-3S) (**M**), control (ctrl) or not depleted (w/o Ab) on CD4 T cells. **D**, **H** and **J** show one representative dose-response experiments among 2-3. (**E-G**, **I**, **K-M**) results are shown as the mean ± SD of the percentage of pSTAT5 NT cells inhibition on 3-4 donors, as indicated. $^{*}p<0.05$, $^{**}p<0.01$ by two tailed unpaired *t*-test (**I** and **K**), $^{***}p<0.001$ by ANOVA with Tukey's correction for multiple comparisons (**E-G**, **L** and **M**).